Roles of wing flexibility and kinematics in flapping wing aerodynamics

Reynolds Addo-Akoto [a], Jong-Seob Han [b], Jae-Hung Han [a],*

[a] *Department of Aerospace Engineering, KAIST, 291 Daehak-ro, Yuseong-gu, Daejeon 34141, Republic of Korea*
[b] *Chair of Aerodynamics and Fluid Mechanics, Technical University of Munich, Boltzmannstr. 15, 85748 Garching, Germany*

A B S T R A C T

Insects are excellent fliers because of their ability to generate precise wing kinematics and deform their wings for the sufficient production of unsteady aerodynamic forces. Most of the previous studies on the effects of wing kinematics on the aerodynamics have been limited to the use of rigid wings, and leaves the contribution of wing flexibility unknown. Here, an experiment was conducted to investigate the effect of varied sweep duration and timing of rotation on the unsteady aerodynamic characteristics of hovering flexible and rigid wings at Re of 10^4. This study found that the forces generated by the flexible wing showed a conspicuous phase delay, which was more sensitive to the change in sweep duration than the timing of rotation. The transient negative lift associated with rigid wings undergoing delayed and advanced wing rotations totally disappeared in the flexible case. A digital particle image velocimetry (DPIV) measurement at the middle of stroke revealed a slight difference in the vortical structures surrounding the two wings in terms of proximity to the shed trailing-edge vortices (TEVs). Also, the linearly twisted nature of the flexible wing caused the coherent leading-edge vortex (LEV) to be stabilized throughout the wingspan. This increased the radial limit of the delayed stall from 3.6c in the rigid wing to 4.8c in the flexible wing. In general, the flexible wing with symmetric and delayed wing rotations generated the higher efficiency. The corresponding net force vectors were tilted in an almost vertical direction in comparison to the rigid wing. This is an indication that natural fliers adopt specific wing kinematics in addition to their wing deformation for the upward titling of their net force vector, which will significantly enhance their aerodynamic performance.

1. Introduction

The long-term hovering, good maneuverability, and light-weight wings of insects and hummingbirds have made them the most efficient fliers (Wootton, 1990). These fliers are capable of overcoming wind gust and object avoidance by adjusting their wing camber and adopting precise wing kinematics (Shyy et al., 2013). Various unsteady mechanisms, which are directly linked to a specific wing motion (Chin and Lentink, 2016), have been found to contribute to the aerodynamic forces (Dickinson et al., 1999). These forces are very sensitivity to the change in wing kinematics, and have attracted much attention in both numerical and experimental studies (Dickinson et al., 1999; Han et al., 2015a; Sun and Tang, 2002).

---

* Corresponding author.
  E-mail address: jaehunghan@kaist.ac.kr (J.-H. Han).

Insect wing motion is governed by numerous parameters such as flapping frequency, deviation, stroke, and pitch amplitudes, timing of rotation, etc. (Sane and Dickinson, 2001; Shyy et al., 2013). In addition, since the motion profile of insects are quite complicated (Ellington, 1984), some studies have proposed simplified analytical and piecewise equations of motion (Berman and Wang, 2007; Sun and Tang, 2002). These approaches have helped to investigate the influence of the individual parameters on the aerodynamic forces. The experimental studies by Sane and Dickinson (2001) using a fruitfly-like wing planform at Reynolds number, Re, of $\sim$100 revealed that lift was maximum when the stroke and pitch amplitudes are 180° and 45°, respectively, with a very short duration of advanced rotation. The sweep motion profile has been reported to influence the overall change in the lift coefficient (Bhat et al., 2020). On the other hand, the pitch motion profile only affects the lift at stroke reversal. All of these works have been limited to a rigid wing for simplicity purpose. However, the presence of wing flexibility has been reported to be essential by re-orienting the aerodynamic forces to enhance the wing's performance during flight (Harbig et al., 2013; Du and Sun, 2008; Zhao et al., 2010).

Few attempts have been made to study the effect of wing kinematics with flexible wing structure (Kang and Shyy, 2013; Dai et al., 2012; Sridhar and Kang, 2015). A numerical study was conducted with a fruit-fly like wing to assess the effect of the timing of rotation (Kang and Shyy, 2013). The variation of the flexibility parameter, frequency ratio, corresponded to a direct change in the timing of rotation. The symmetric wing rotation was reported to be optimum, and even generated higher lift than the rigid wing by mitigating the downwash. This study was limited to a two-dimensional (2D) wing at Re of 100 because at such low Re the spanwise effect is of less importance (Birch and Dickinson, 2001; Shyy and Liu, 2007). However, another numerical study also conducted at low Re with a 3D flexible membrane attached to a stiff leading edge (LE) vein revealed that the 3D wing deformation might have a significant effect on the spanwise flow. The warping of the wing created an impedance effect by concentrating the spanwise flow near the wing tip (Dai et al., 2012).

One key observation is that the wing design, consisting of LE vein and flexible membrane only, in the above study generates a negatively-cambered wing, which has been reported to have a poor aerodynamic performance (Ryu et al., 2019; Harbig et al., 2013). The generation of the negative wing camber in the previous works is contrary to the positive wing camber and linear twist reported in insect's wing deformation (O'Hara and Palazotto, 2012; Walker et al., 2010; Young et al., 2009). Some attempts have been made to investigate the effect of positive camber and linear twist (Du and Sun, 2008, 2010; Harbig et al., 2013). The presence of positive camber alone has been reported to enhance the lift by accelerating more of the flow at the suction side of the wing compared to that of a flat wing. This creates a further decrease in pressure at the suction side to augment the lift, and causes the pressure forces to act more in the vertical direction (Harbig et al., 2013; Du and Sun, 2010). Linear twist on the other hand has been reported to cause a decrease in only the required aerodynamic power (Phan et al., 2017a; Du and Sun, 2010; Nakata and Liu, 2012). Nevertheless, a combination of both deformations increased lift by 10%, reduced drag by 4%, reduced aerodynamic power by 5%, and increased the overall efficiency by 17% in comparison with a rigid wing (Du and Sun, 2010).

Based on the aforementioned studies, the combination of positive camber and linear twist are essential for the full comprehension of the flow-dominated field around an insect-like flapping wing. First, it should be noted that all of the above studies on camber and twist have been conducted at low Re ($\sim$10^2). However, the bursting of the LEV at intermediate Re (10^3–10^4) results in more complicated substructures (Garmann et al., 2013). Therefore, much effort is required to analyze the 3D vortical structures around a wing with camber and twist at such high Re. This makes the estimation of the aerodynamic forces to be quite difficult at that Re regime. In addition, since previous works (Du and Sun, 2008, 2010; Harbig et al., 2013) have simplified their wing deformation by using the analytically pre-determined camber and twist, a more realistic analysis of the wing deformation caused by the fluid–structure interaction (FSI) is essential. Allowing the wing to be fully deformed by the surrounding fluid will be more beneficial, realistic, and applicable for designing flapping wing micro-aerial vehicles (FWMAVs) since the Re regime is also suitable for that application.

Some recently developed FWMAVs have been able to achieve positive camber and linear twist deformations during the flapping of their wings (Phan et al., 2017b; Nan et al., 2017; Roshanbin et al., 2017, 2019; Nguyen and Chan, 2019). However, there is a knowledge gap in terms of how the camber and twist affects the 3D vortical structures, and help enhance the lift. Therefore, a comprehensive analysis of the vortical structures will help to fully explore the disadvantages and advantages of flexible wing design in FWMAVs. Lastly, most of the studies have been limited to symmetric wing rotation, however, natural flyers use either delayed or symmetric wing rotation during hovering flight (Walker et al., 2010; Fry et al., 2005). Therefore, it is paramount to study the wing kinematics effect at such high Re using a flexible wing capable of exhibiting positive camber and linear twist.

In this paper, an experiment was conducted to investigate the effect of sweep motion profile and timing of rotation of a flexible flapping wing on the aerodynamic performance. A scaled-up robotic model was used to precisely obtain the wing kinematics. A total of 30 experimental results were obtained from the combination of five different sweep motion profiles and three timing of rotations with flexible and rigid wings. The rigid wing was included to better understand the role of wing deformation. The instantaneous vortical structures responsible for the measured aerodynamic forces were observed using a digital particle image velocimetry (DPIV) measurement technique. The examination of the aerodynamic forces and vortical structures at Re of $\sim$10^4 implies that the results from this study will be helpful in the design of the flapping mechanisms of FWMAVs.
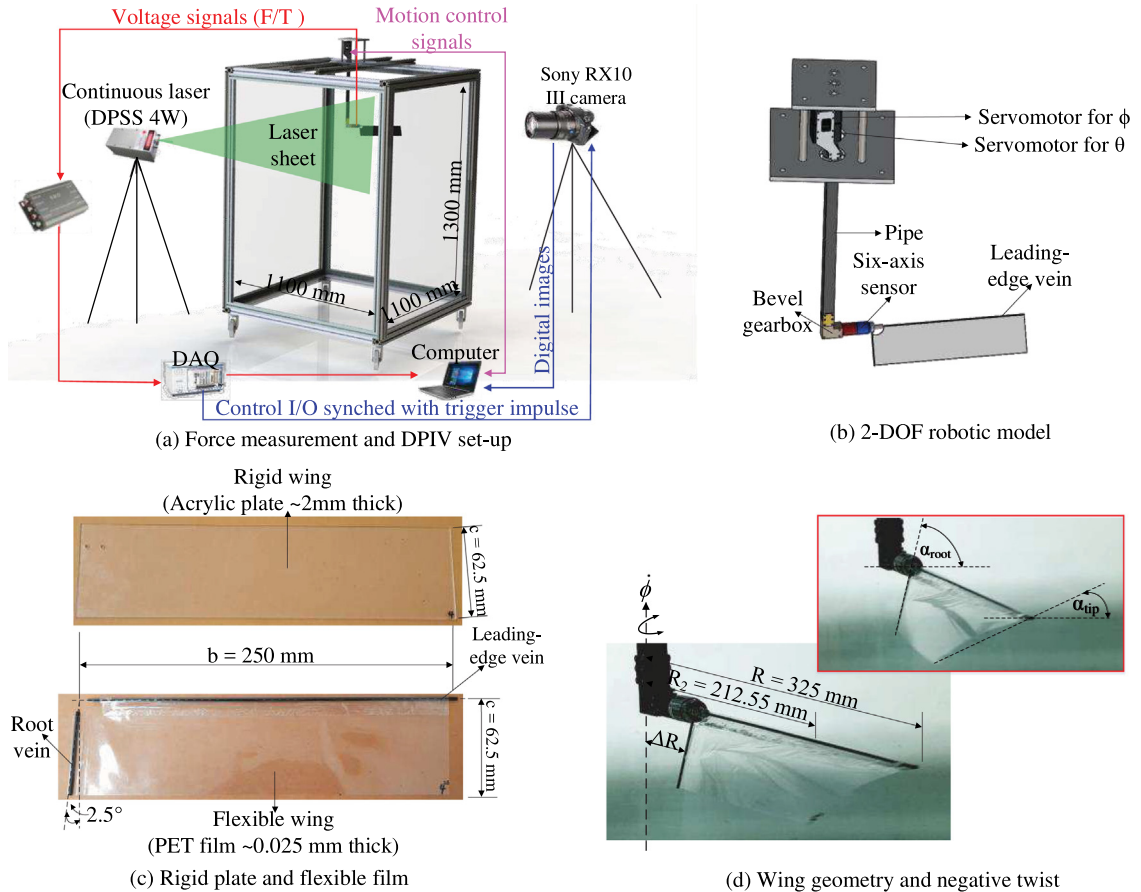
(a) Force measurement and DPIV set-up

(b) 2-DOF robotic model

(c) Rigid plate and flexible film

(d) Wing geometry and negative twist

Fig. 1. Experimental set-up for force/moment and DPIV measurements with wing geometry.

2. Materials and method

2.1. Experimental set-up

The complete experimental set-up for the measurement of the aerodynamic forces /moments, and visualization of the vortical structures is shown in Fig. 1. The water tank has a length, width, and height of 1.1 m, 1.1 m, and 1.3 m, respectively. A two degree-of-freedom (2-DOF) dynamically scaled-up robotic model was used to generate the continuous back-and-forth movement of the wing. The 2-DOF motion comprised of pitch and sweep motions with an angle of θ and ϕ, respectively. These motions were independently achieved with two servo motors (XH430-210R, ROBOTIS Inc.) as shown in Fig. 1(b). An in-house code was used to transmit the motion control signals from a computer to the two motors in a sequential manner as shown in Fig. 1(a). The detailed construction of the model has been provided in our previous study (Han et al., 2019). A six-axis sensor (NANO17-IP68) of measurement range ± 12 N and ± 120 N-mm was placed at the wing root to measure the forces and moments.

The geometric definitions of the wing are shown in Fig. 1(c). A rectangular wing of span length b 250 mm and chord length c of 62.5 mm was selected. This gave an aspect ratio AR value of 4, which is the maximum limit needed for the delayed stall to be effective (Kruyt et al., 2015). The characteristic distance R between the flapping axis and wing tip was $\sim$325 mm. This resulted in a distance of 225 mm between the wingtip and the wall of the tank; sufficiently enough to avoid the wall effect (Dickinson et al., 1999). In addition, the distance between the wing and the floor of the tank was $\sim$14c. This distance is also enough to overcome the ground effect since this effect disappears after $\sim$3c (Kweon and Choi, 2012). The wing root offset ΔR of 75 mm placed the location of the non-dimensionalized radius of gyration $\hat{r}_2 = R_2/R$, which is the ratio between the distance of the radius of gyration R_2 and the characteristic length R, at 0.654.

In order for the flexible wing deformation to exhibit the positive camber and linear twist, the same concept deployed in designing the wings of existing FWMAVs was adopted (Phan et al., 2017b; Nan et al., 2017; Nguyen and Chan, 2019). Two veins were each placed at the wing's LE and root with an offset at the wing root, which is called slack angle, as shown in Fig. 1(c). This wing configuration causes the angle of attack at the wing root α_{root} to be greater than that at the
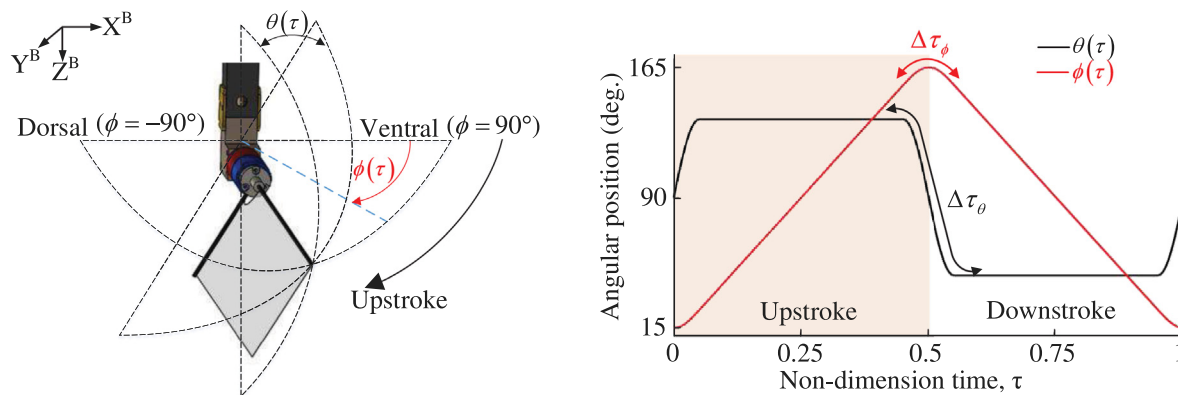
Fig. 2. Wing kinematic parameters and definitions.

wing tip α_{tip} as seen in the insert in Fig. 1(d), which is known as the negative wing twist effect. Also, the buckling of the wing during stroke reversal means that there is an interplay between buckling and wing twist during the wing motion. A slack angle of 2.5° was selected because it has been reported to generate the maximum lift among other slack angles with the same wing configuration (Addo-Akoto et al., 2020). A detailed procedure for the construction of the flexible wing has been provided in our previous studies (Addo-Akoto et al., 2020). The flexible and rigid wings were made of 25 μm thick PET film and 2 mm thick acrylic plate, respectively. The presence of very stiff LE and root veins in the design of flapping wings have separately been reported to help enhance the aerodynamic performance in comparison with wings having uniform stiffness (Nguyen et al., 2016; Wang et al., 2017). Therefore, a 2 mm carbon rod with ∼49 times the stiffness of the PET film was selected to fabricate the veins. The flexural stiffness $EI = Ebt^3/12$ was ∼1.53×10^{-6}N-mm ^{2} and ∼0.53 N-mm ^{2} for the flexible and rigid wings, respectively. The very low stiffness of the flexible wing indicates that it can easily be deformed by the fluid. The non-dimensional effective stiffness (Π_1), which measures the ratio of elastic bending to fluid dynamic forces (Fu et al., 2018; Shyy et al., 2010), was 757 and 0.0022 for the rigid and flexible wings, respectively. These values further indicate that the fluid forces were responsible for the deformation of the flexible wing while the rigid wing had enough bending stiffness to withstand any deformation by the fluid forces. Similarly, the density ratio, which is the ratio between the wing and fluid densities, was 1.22 and 2.02 for the rigid and flexible wings, respectively. An indication that the fluid forces were more dominant in the low-density-ratio system in this study.

2.2. Wing kinematics

Fig. 2 explains how the wing kinematic parameters were defined. The piecewise wing kinematics proposed by Sun and Tang (2002) and deployed in our previous studies (Han et al., 2019; Addo-Akoto et al., 2019) was adopted in this study. The non-dimensionalized time τ was defined as $\tau = t/T$, where t is the actual time elapsed and T is the total time for one complete flapping cycle. The sweep motion profile $\phi(\tau)$ basically consisted of two parameters namely the non-dimensional sweep duration $\Delta\tau_\phi$ and the sweep amplitude ϕ_{amp}. On the other hand, the pitch motion profile $\theta(\tau)$ consisted of the non-dimensional pitch duration $\Delta\tau_\theta$, timing of rotation $\Delta\tau_R$, and the pitch amplitude θ_{amp}. Based on the body coordinate system, the wing sweeps and pitches along the Z and Y axes, respectively.

Fig. 3 describes the angular positions and velocities based on the varied parameters for the sweep and pitch motions. The sweep motion profile was varied by changing $\Delta\tau_\phi$ from 0.1 to 0.5. This changed the sweep velocity profile from a near constant to sinusoidal shape as shown in Fig. 3(c). In terms of the pitch motion variation, $\Delta\tau_\theta$ has been reported to have less effect on the alteration of the aerodynamic characteristics (Bhat et al., 2020). Therefore, $\Delta\tau_\theta$ was fixed at 0.16 while $\Delta\tau_R$ was varied at 0, −0.08, and 0.08 (Dickinson et al., 1999) to represent the three insect wing rotations, symmetric, advanced, and delayed rotations (Walker et al., 2010; Fry et al., 2005), respectively. It should be noted that the range of motion profiles selected in this study also covers that of some natural fliers (Liu and Sun, 2008; Altshuler et al., 2005) and FWMAVs (Phan et al., 2017b; Roshanbin et al., 2019) in hover.

The rigid wing was pitched at ±45° while the flexible wing was at ±15° based on our previous studies (Addo-Akoto et al., 2020). The twisting effect causes the sectional angles of attack to linearly decrease across the wing span from the wing root to the wing tip (Addo-Akoto et al., 2021). With this feature, both the rigid and flexible wings had similar geometric angle of attack at their respective R_2 during the middle of stroke. Although research has shown that the pitching axis for flapping wings lie at 1/2c (Han et al., 2015b), the constraint in the configuration of the flexible wing only allowed the wing to be pitched at the leading edge as shown in Fig. 1d. The flapping frequency f of 0.1 Hz and sweep amplitude ϕ_{amp} of 150° gave Re value of ∼1.1×10^4 based on Eq. (1). This Re value could be equivalent to an estimated weight of ∼5.2 g for flapper in hover (Han et al., 2014). In addition, the selected Re was enough to induce the bursting and stabilization of the LEV (Lu et al., 2006; Kruyt et al., 2015). The sweep velocity and pitch velocity were normalized as $\dot{\phi}^* = \dot{\phi}/\bar{\dot{\phi}}$ and
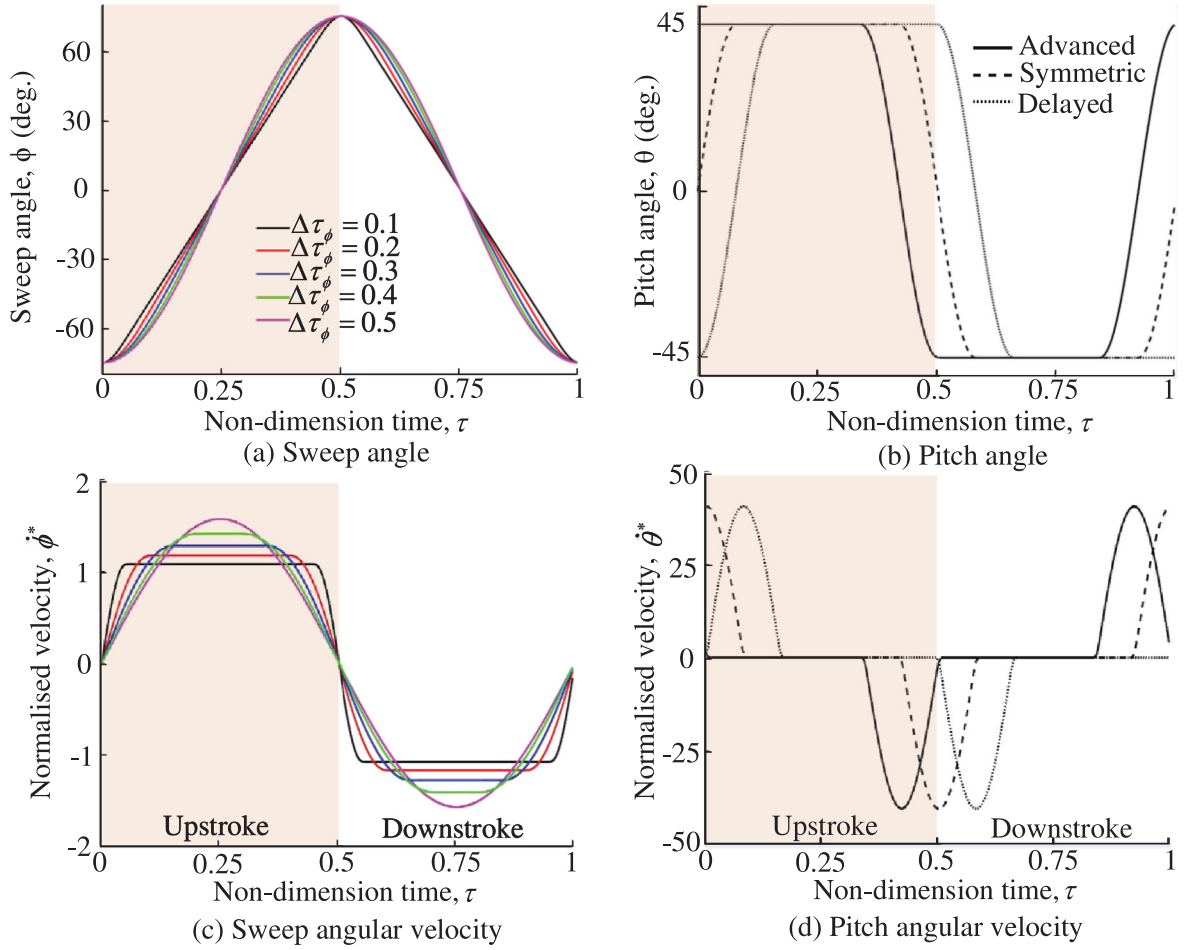
Fig. 3. Angular position and velocity based on variations of the sweep and pitch motion parameters.

$\dot{\theta}^* = \dot{\theta}c/\overline{U}_{ref}$, respectively, as shown in Fig. 3(c) and (d). The reference velocity defined as the wingbeat-cycle-averaged velocity at the location of the radius of gyration R_2 as $U_{ref} = 2\overline{\phi}fR_2$.

$$\text{Re} = \frac{2f\phi_{amp}Rc}{\nu} \tag{1}$$

2.3. Measurements

Experiments were first conducted to measure the aerodynamic forces, and then the corresponding vortical structures were observed using the digital particle image velocimetry (DPIV) technique. A single run LABVIEW[TM] code made of five continuous flapping cycles were used as shown in Fig. 4. These five cycles were enough to avert the underdeveloped wake effect (Birch and Dickinson, 2003). A rest period of ~10 flapping cycles (100 s) was included to generate quiescent flow, and eliminate any possible recirculation flow for inaccurate measurement. This entire process was repeated for 20 iterations for the convergence of the ensemble average. The examination of the aerodynamic characteristics in this study was conducted during the fifth flapping cycle.

The measurement uncertainty along the ϕ and θ axes were 0.059% (150°±0.088°) and 0.38% (90°±0.088°±0.25°), respectively, where the tolerance for the gearbox was ±0.25° and servomotor was ±0.088° as provided by the manufacturer. The use of five millisecond update time based on the 2000 digitized data points in a unit wingbeat cycle generated a precision error of 0.05% (1/2000). The negligible variation in the temperature of the water around 19.8 ±0.2°C led to the change in density to be ± 0.008%. The sensor resolutions of 1/64 N-mm and 1/320 N also generated a precision error of 0.33% and 0.21% based on the maximum amplitudes of the force and moment measurements, respectively. These uncertainties were assessed based on the measurements with the rigid wing; maximum loading. The total systematic uncertainty was 1.04%.
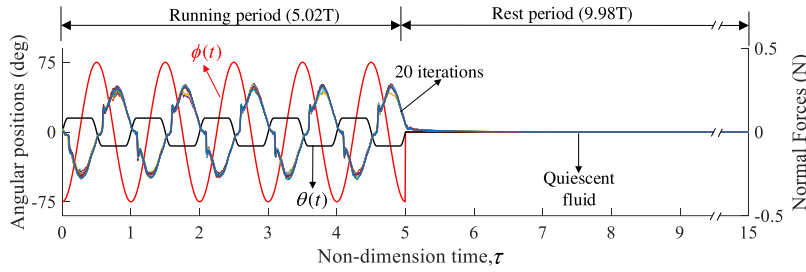
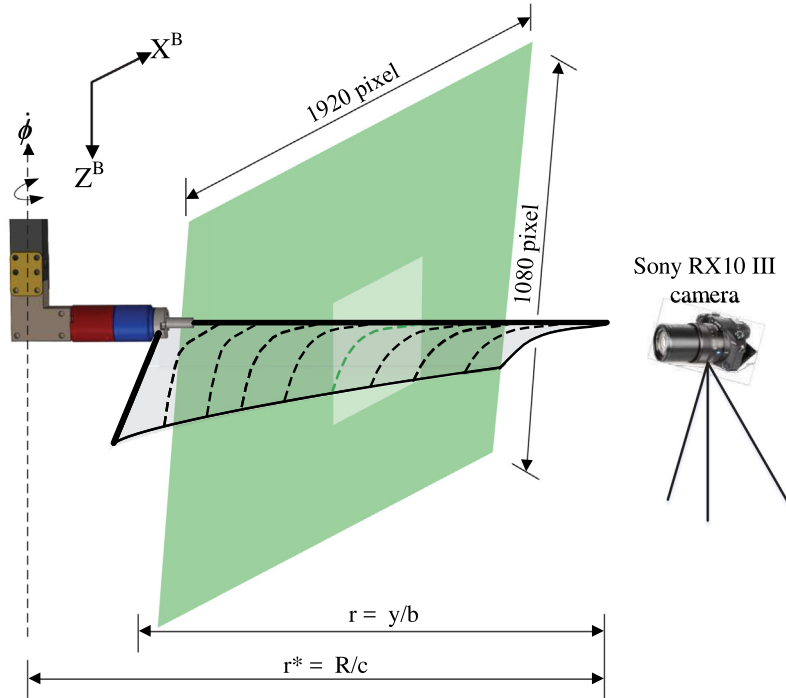Fig. 4. Measured normal forces and motion profile for the flexible wing.

Fig. 5. Schematic wing deformation with DPIV set-up.

Fig. 5 shows a schematic drawing of the DPIV set-up, which consisted of a continuous laser and a high-speed camera, and the deformation of the wing as it penetrated the field of view (FOV). The camera recorded the particle motion for a period of $\Delta\tau = 0.04$ as the wing passed through the 1920 (H) × 1080 (W) FOV. This recording period was enough to capture the instantaneous vortical structures at $\tau = 4.60$ and 4.75 (to be discussed later in details). The recordings were acquired with a 50 mm, ISO 800 lens with 250 frames/s shutter speed. The diameter of the Polymethyl methacrylate (PMMA) particles was 100 μm. Ten individual chord-wise cross-sections were taken to reveal the 3D vortical structures from 0.1b to 1.0b with 0.1b interval. The recording at each cross-section was repeated 20 times yielding a total of 100 pairs of image from the five flapping cycles. The FOV had a resolution of 107 × 191 from a 40 × 40 interrogation area with 50% overlap. The flow velocity vectors were extracted using the open-source code in MATLAB, PIVLAB (Thielicke and Stamhuis, 2014). The uncertainty of the DPIV measurement had a maximum error of 0.0815 pixel based on the correlation statics approach (Wieneke, 2015). This corresponded to a maximum particle displacement of 3.5%.

In Section 3 of this study, the time-varying aerodynamic force characteristics of the rigid and flexible wings were examined based on the variation of $\Delta\tau_\phi$. Each variation was performed for advanced, symmetric, and delayed wing rotations. For a wing with linear twist, an approximately zero lift is generated when the geometric angle of attack α_{geom} at $\hat{r}_2$ is zero (Du and Sun, 2008). Therefore, it is appropriate to calculate the lift using the velocity at $\hat{r}_2$ as the reference velocity U_{ref} for the flexible wing. The same location has also been reported to be suitable for wings with constant angle of attack (Lua et al., 2014). This means that the velocity at $\hat{r}_2$ is the appropriate scaling velocity for both wings. Eqs. (2)

and (3) were used to calculate the coefficient of lift C_L and drag C_D.

$$C_L = \frac{2L}{\rho U^2_{ref} S} \tag{2}$$

$$C_D = \frac{2D}{\rho U^2_{ref} S} \tag{3}$$

3. Aerodynamic force characteristics

3.1. Effect of varied sweep motion profile

Fig. 6 shows the time-course forces for the two wings with advanced wing rotation during the fifth flapping cycle. One noteworthy feature is the generation of negative lift for the rigid wing. This feature occurs because the early rotation of the wing ($4.342 \leq \tau \leq 4.502$) prior to stroke reversal tends to increase the α_{geom} from 45° to 135° in the direction of motion, and results in the negative lift generation (using $C_L \approx \sin 2\alpha_{geom}$). Thus, the wing generates zero lift at 90° and negative lift afterwards. The negative lift feature is very common for rigid wings undergoing advanced wing rotation (Sane and Dickinson, 2002; Ramamurti and Sandberg, 2002; Dickinson et al., 1999). This study has found that an increase in $\Delta\tau_\phi$ can reduce the magnitude of the negative lift by ~62%. The increase in $\Delta\tau_\phi$ caused a reduction in the sweep velocity of the wing during the deceleration phase of motion. For instance, at $\tau = 4.45$ the minimum C_L was generated, and the non-dimensional sweep velocities of the wing for $\Delta\tau_\phi = 0.1$ and 0.5 were 1.08 and 0.49, respectively. That was 55% reduction in velocity and led to the observed drastic reduction in the magnitude of the negative lift. A proper modulation
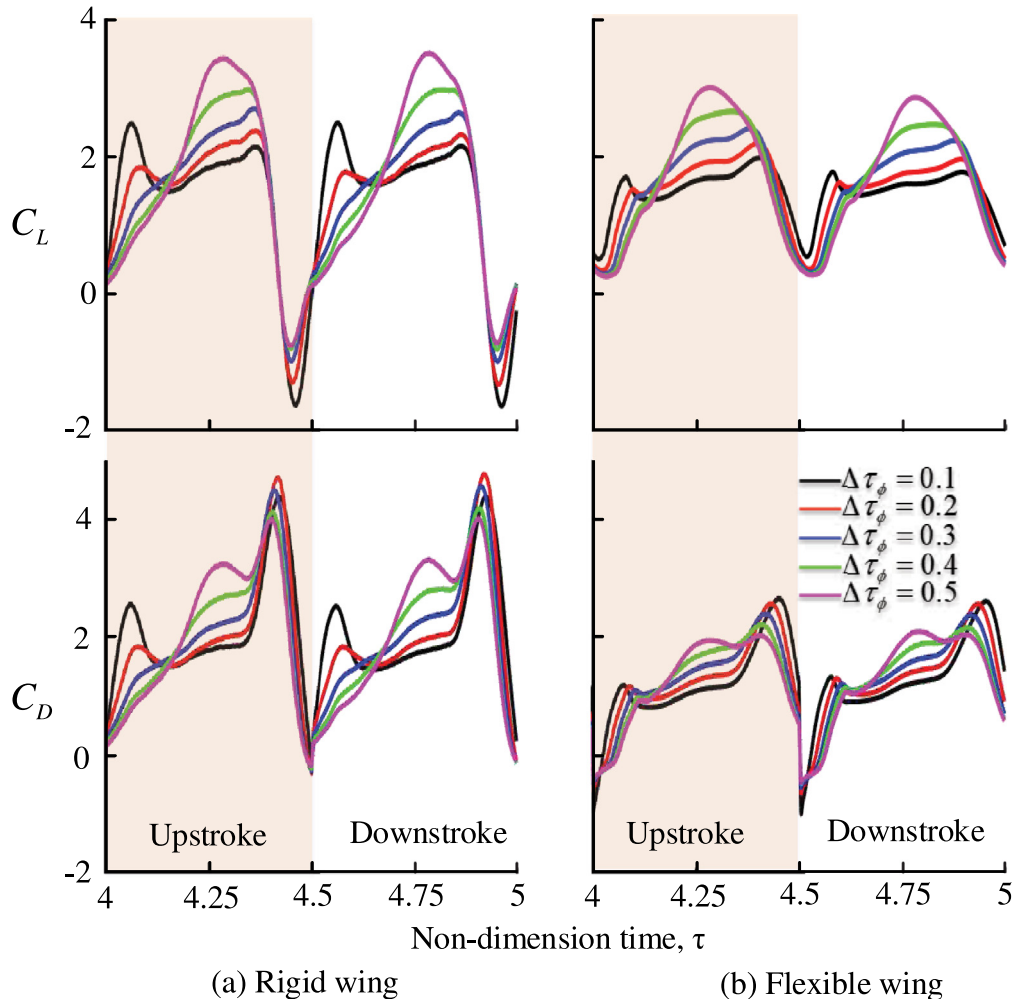

Fig. 6. Time-varying forces in the fifth cycle for advanced wing rotation based on varied sweep motion profile.
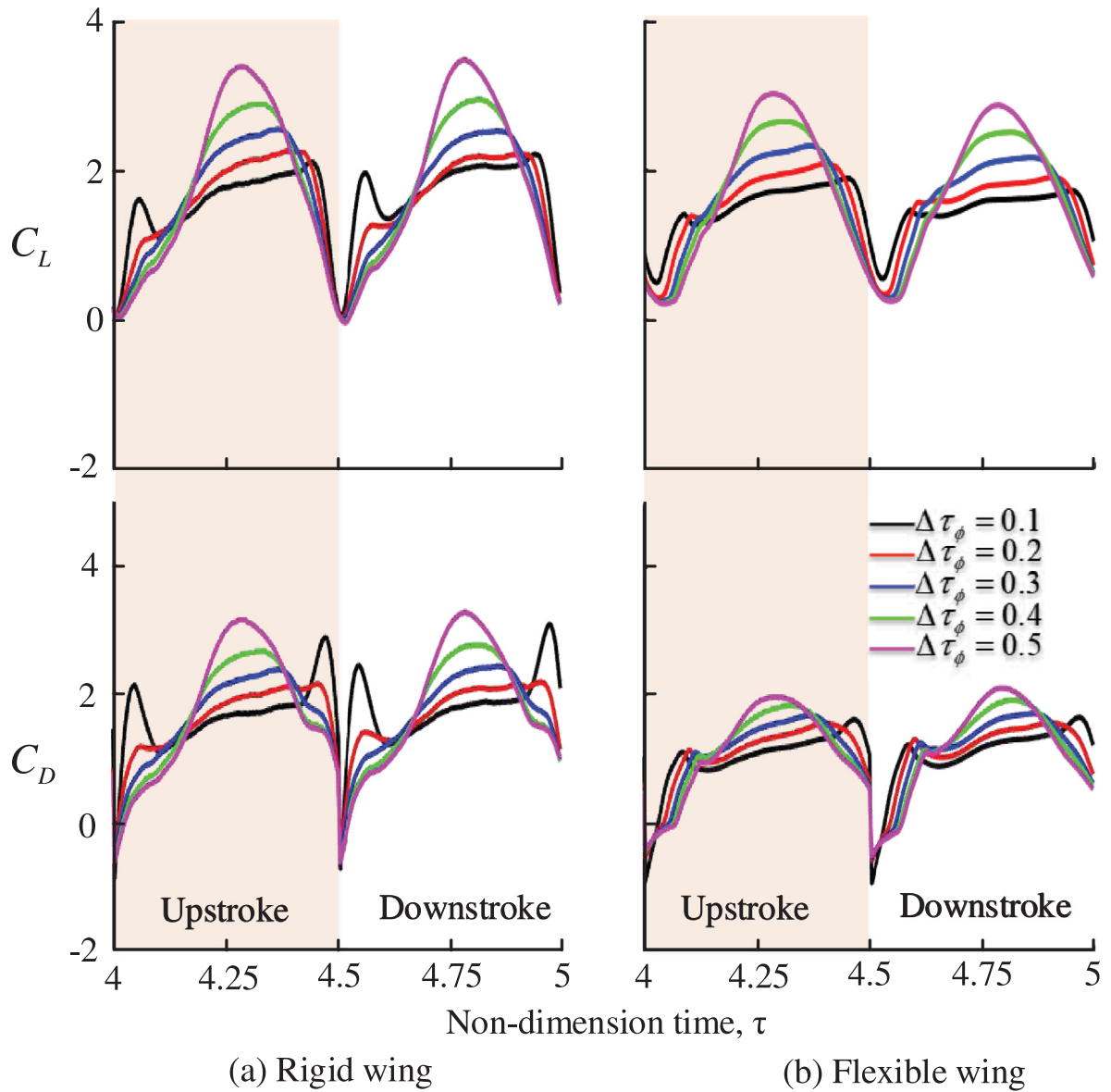
Fig. 7. Time-varying forces in the fifth cycle for symmetric wing rotation based on varied sweep motion profile.

of the decelerating velocity could be a good approach to reduce the magnitude of the negative lift. On the other hand, the generation of the negative lift totally disappeared for the flexible wing. The same observation could not be found for the flexible wing with only LE vein undergoing sinusoidal motion (Dai et al., 2012). This indicates that the inclusion of the wing-root vein, which helps to generate the positive camber, might play a key role in eliminating the negative lift, and has a better advantage for FWMAV applications. In addition, a conspicuous phase delay in force generation occurred as $\Delta\tau_\phi$ was increased. Thus, the flexible wing behaved as if it were rather undergoing delayed rotation. Generally, an increase in $\Delta\tau_\phi$ increased the lift and drag at the middle of each half stroke ($\tau = 4.25$ and 4.750), and decreased the peak forces observed immediately after stroke reversal, which could be caused by the wake-capture (Dickinson et al., 1999; Addo-Akoto et al., 2019; Han et al., 2015a,b) and/or added-mass effects (Sun and Tang, 2002). Since the time appearance of the peak force for the flexible wing varied as $\Delta\tau_\phi$ increased, further studies will be required to elucidate the reason for that behavior.

The aerodynamic force characteristics of the rigid wing undergoing symmetric rotation does not show any negative lift generation as displayed in Fig. 7. Rather, the wing generated an almost zero lift at the end of stroke ($\tau = 4.50$), which was due to the 90° attitude of the wing. Also, it could be seen that a change in $\Delta\tau_\phi$ had no effect on the lift at that instant time. However, the flexible wing at that time instant generated an appreciable amount of minimum C_L. The amount of lift
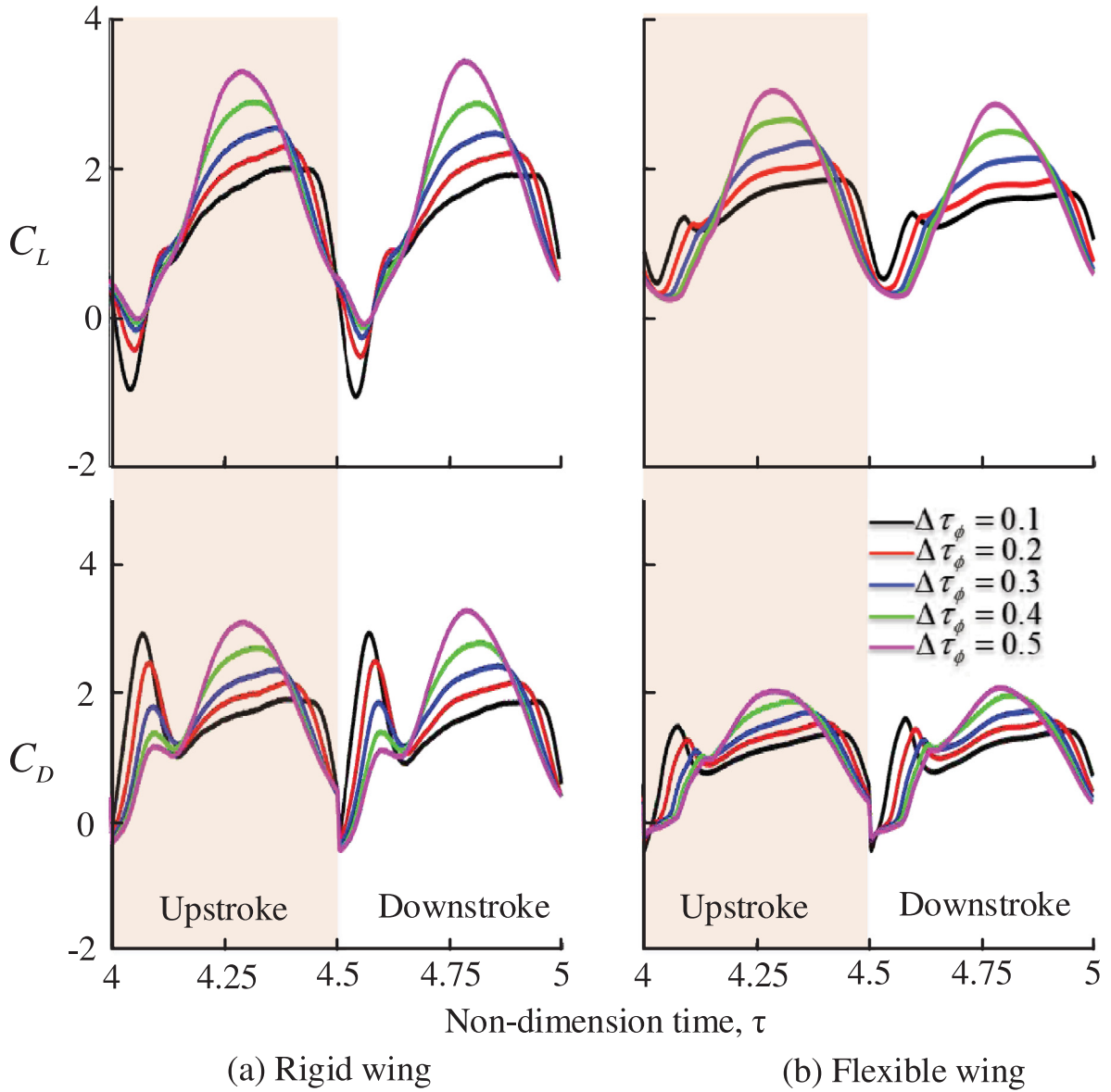
Fig. 8. Time-varying forces in the fifth cycle for delayed wing rotation based on varied sweep motion profile.

at that instant was significantly affected by $\Delta\tau_\phi$. A change in $\Delta\tau_\phi$ from 0.1 to 0.5 reduced the lift from 1.16 to 0.58, which was about 50% reduction. Comparing the lift behavior here to the velocity plot in Fig. 3(c), it could be seen that the shape of the lift graph tends to take the same form as the velocity plot. Thus, the lift plateau associated with the triangular sweep motion ($\Delta\tau_\phi = 0.1$) could be seen to have occurred due to the long period of constant velocity ($4.05 \leq \tau \leq 4.45$) while a sinusoidal lift profile was generated by the sinusoidal sweep motion ($\Delta\tau_\phi = 0.5$) for both wings. The peak force, which might be due to the wake-capture and translational acceleration of the wing, was very conspicuous in this case as $\Delta\tau_\phi$ decreased for both wings.

Delayed wing rotation implied that the wing rotated after stroke reversal ($4.51 \leq \tau \leq 4.67$). The flexible and rigid wings now showed similar trend in force behavior as shown in Fig. 8 where the force valley in both cases occurred after stroke reversal. The attitude of the rigid wing in the direction of motion also contributed to the generation of the negative lift in this case as shown in Fig. 8(a) (explanation already given). The major difference in the negative lift generation between the advanced and delayed rotation is the timing of its appearance; before or after stroke reversal. One key observation made here was that the increase in $\Delta\tau_\phi$ for the rigid wing rather helped to eliminate the negative lift when $\Delta\tau_\phi$ was 0.4 and 0.5. This shows that with the proper selection of $\Delta\tau_\phi$, the negative lift that has been reported for delayed wing rotation in previous studies (Sane and Dickinson, 2002; Ramamurti and Sandberg, 2002; Dickinson et al., 1999) could

be eliminated. The flexible wing generated a positive minimum lift irrespective of $\Delta\tau_\phi$ in this case too. Also, the peak force due to the wake-capture was inconspicuous irrespective of the change in $\Delta\tau_\phi$ for the rigid wing.

3.2. Effect of timing of rotation

This study has so far established that the flexible wing generated positive transient lift throughout the wing motion, and the phase delay in force generation is very sensitive to the variation of $\Delta\tau_\phi$ irrespective of the timing of rotation. But the extent to which the timing of rotation also affects the observed phase delay could not be clearly estimated. Therefore, the aerodynamic characteristics were re-constructed into a single plot for the triangular ($\Delta\tau_\phi = 0.1$) and sinusoidal ($\Delta\tau_\phi = 0.5$) sweep motion to better understand this effect.

The plot in Fig. 9 shows that the effect of the timing of rotation has a significant effect on the rigid wing regardless of $\Delta\tau_\phi$ by changing the locations of the appearance of the negative lift. After the wing had finished pitching, the forces then converged to the same magnitude due to the attainment of the same sweep velocity and α_{geom} by the wing. The wing in
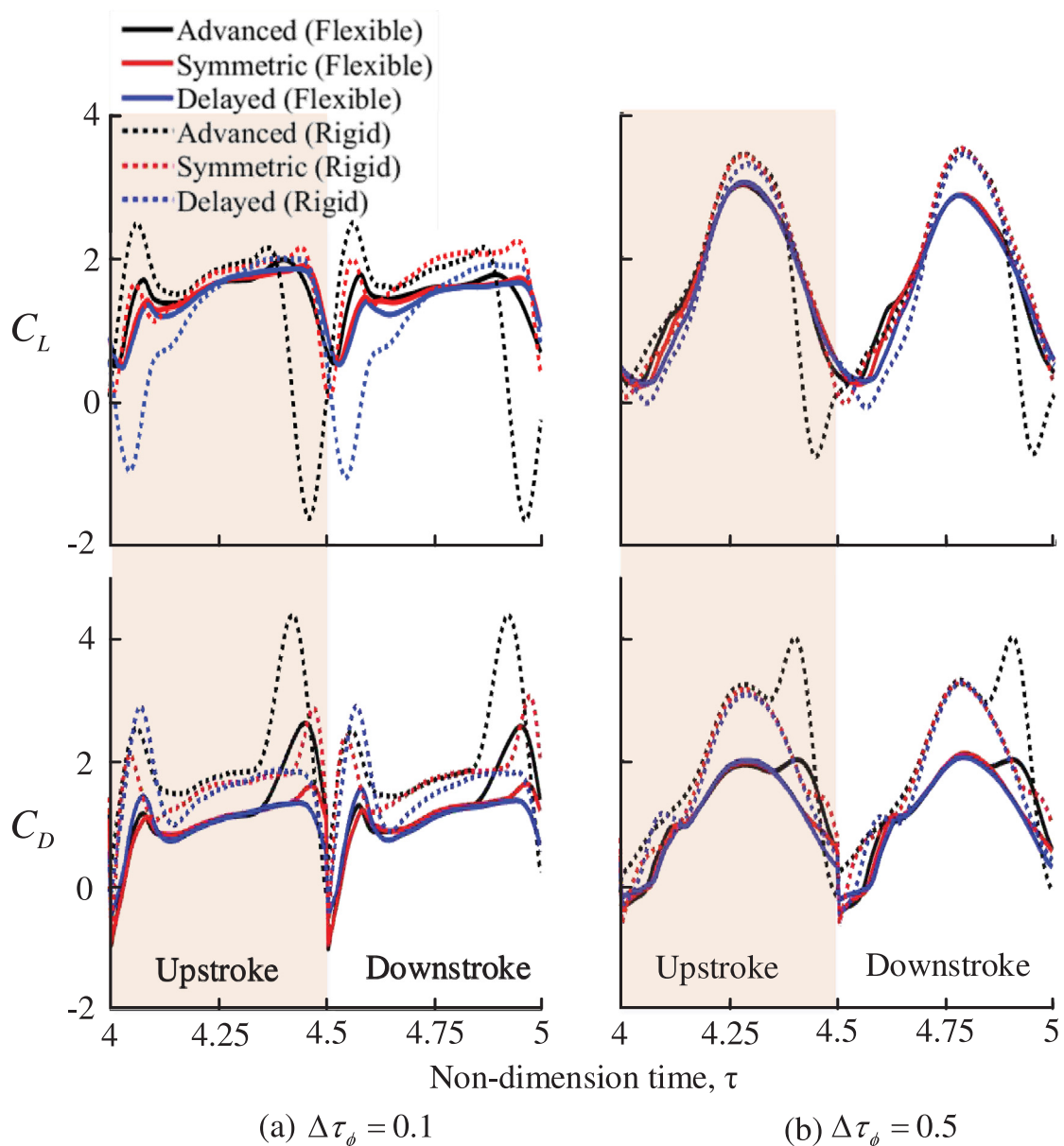

Fig. 9. Time-course of forces in the fifth cycle based on varied timing of rotation.

advanced rotation benefited significantly from the wake-capture irrespective of the wing flexibility. The complete pitching of the wing in the previous stroke increased the effective flow velocity, and upon stroke reversal the wing encountered the strong wake, which caused the sharp peak force. The contribution of the wake-capture force was drastically reduced with $\Delta\tau_\phi = 0.5$ for both wings too.

Another noteworthy observation is that the magnitude of the positive minimum lift generated during stroke reversal for the flexible wing remained the same regardless of the timing of rotation. This might be caused by the dissipation of the elastic energy during the stroke reversal (Reid et al., 2019; Nakata and Liu, 2012). This elastic energy, which is stored in the form of camber and twist, has been reported to aid the flexible wing catch up with the lift generated by the rigid wing in order to overcome the effect of the phase delay (Nakata and Liu, 2012). The transition of the flexible wing from forward to back stroke also causes the wing to generate some form of buckling behavior. Further studies will be needed to really address the causative factor(s) in cases like these where the wing could generate similar magnitude of minimum lift during this transition phase even for advanced and symmetric wing rotations. The variation in $\Delta\tau_\phi$ has significant effect on the magnitude of the lift than τ_R (refer to Figs. 6 to 8). In this regard, the very low lift generated during stroke reversal by the sinusoidal sweep motion could be as a result of the very slow dissipation of the elastic energy and lower wing speed at stroke reversal.

Furthermore, the linear twist causes the distal wing area to have a relatively delayed sweep angle in comparison to the wing base area (Nakata and Liu, 2012). This relative delay in sweep angle induced the observed delay in the entire aerodynamic characteristics of the flexible wing in this study. The phase delay could also be a reflection of the passive dynamics of the inertial of the wing (Ennos, 1988). Based on the above explanations, $\Delta\tau_\phi$ is the key parameter to determine the degree of phase delay, and the magnitude of the lift during stroke reversal for the flexible wing.

4. Mean aerodynamic forces, efficiency, and net force vector

4.1. Mean C_L, C_D C_{PW} and η

The cycle-averaged values of the fifth flapping cycle ($4 \leq \tau \leq 5$) were evaluated for C_L, C_D, and efficiency η. The use of $\overline{C}_L/\overline{C}_D$ to evaluate the efficiency of flapping wing is not adequate enough to account for the total rate of energy consumed by the combined pitching and sweeping motions (Nguyen et al., 2016). Therefore, the most suitable way to evaluate the efficiency of the wing is by considering the ratio of lift to aerodynamic power P. The power coefficient C_{PW} fully takes into account the total rate of work done by the wing as presented in Eqs. (4) and (5). This calculation came from the sum of the product of the angular velocity and moment about the two motion axes. The efficiency η estimation of the wing is presented in Eq. (6).

$$P = M_\theta \omega_\theta + M_\phi \omega_\phi \tag{4}$$

$$C_{PW} = \frac{2P}{\rho U^3_{ref} S} \tag{5}$$

$$\eta = \frac{L}{P} = \frac{C_L}{C_{PW} U_{ref}} \tag{6}$$

The results in Fig. 10(a) show that an increase in $\Delta\tau_\phi$ generally increases the lift. This supports the findings from previous studies (Bhat et al., 2020; Han et al., 2019; Nabawy and Crowther, 2015) on the effect of $\Delta\tau_\phi$ for the rigid wing undergoing symmetric rotation. Nevertheless, this study has further revealed that the finding remains the same irrespective of the timing of rotation and degree of flexibility. The rigid wing undergoing symmetric rotation generated the highest lift for each value of $\Delta\tau_\phi$ in this study. The increase in $\Delta\tau_\phi$ from 0.1 to 0.5 increased the lift by 20.23%, 10.78%, and 44.68% for the advanced, symmetric, and delayed rotations for the rigid wing. This implies that the variation in $\Delta\tau_\phi$ is more beneficial when delayed rotation is deployed. The advanced rotation in this study could not generate the highest lift as reported in previous work (Dickinson et al., 1999) because the very short $\Delta\tau_\theta$ deployed in this study further increased the magnitude of the negative lift. The magnitude of the peak force due to the wake-capture was not high enough to counteract the strong negative lift effect.

The flexible wing undergoing symmetric and advanced rotation generated almost the same amount of lift for each $\Delta\tau_\phi$ with a maximum difference of ~1.45%. The flexible wing could generate more lift than the rigid wing with these 2 rotations for all values of $\Delta\tau_\phi$. The variation of $\Delta\tau_\phi$ from 0.1 to 0.5 for the flexible wing also increased the lift by 11.23%, 14.21%, and 13.78% for the advanced, symmetric, and delayed rotations, respectively. The high lift generation associated with the sinusoidal sweep motion ($\Delta\tau_\phi = 0.5$) could be the reason for its adoption in the flight of some natural fliers (Liu and Sun, 2008) and FWMAVs (Roshanbin et al., 2019; Nguyen and Chan, 2019).

The variation in $\Delta\tau_\phi$ caused a minimal effect on the drag as seen in Fig. 10(b). But the timing of rotation had a significant effect where the advanced rotation generated the highest drag for both wings. The power consumption for both wings displayed the same trend as observed in Fig. 10(c). The power consumption increased as $\Delta\tau_\phi$ increased with advanced rotation consuming the highest power followed by symmetric and delayed rotations. The symmetric rotation was the most efficient for each value of $\Delta\tau_\phi$ among the rigid cases. However, the flexible wing was more efficient than the rigid wing in all cases as shown in Fig. 10(d) with delayed rotation being the most efficient. But there was not much difference
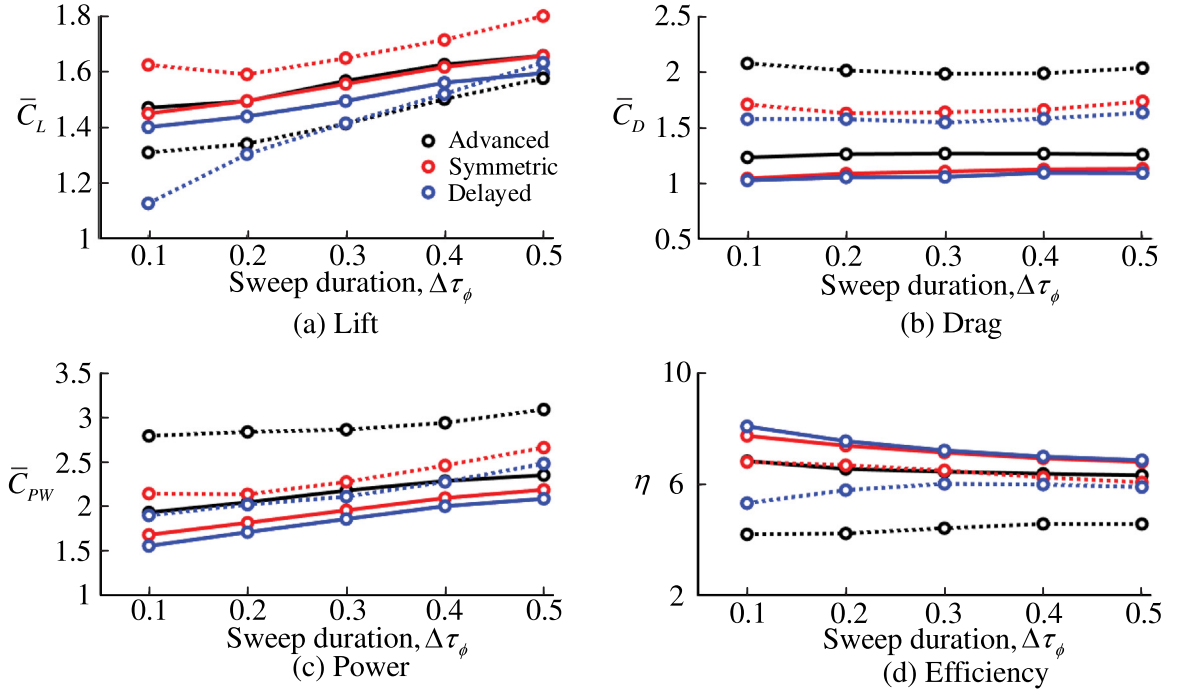
Fig. 10. Cycle-averaged forces, power, and efficiency in the fifth cycle for the rigid (dash lines) and flexible (solid lines) wings.

in efficiency between the delayed and symmetric rotations displayed; ∼0.94% to ∼4.4% difference. This could indirectly explain why hoverflies use a combination of delayed and symmetric rotation (Walker et al., 2010), and fruit-flies adopt delayed rotation to overcome headwind gust during hover (Gu et al., 2020). In terms of $\Delta\tau_\phi$, the triangular sweep motion ($\Delta\tau_\phi = 0.1$) generated the highest efficiency for all the flexible cases. Same observation was made for the rigid wing only in symmetric case, and agrees with literature (Bhat et al., 2020; Han et al., 2019; Nabawy and Crowther, 2015). The rigid wing with delayed and advanced rotations rather required large $\Delta\tau_\phi$ to be efficient. Since flexible wings are more applicable in FWMAVs, the proper adjusting of $\Delta\tau_\phi$ with symmetric rotation is recommended to augment the aerodynamic performance.

4.2. Net force vector and angle

The instantaneous net forces were calculated using $C_F = \sqrt{C^2_L + C^2_D}$, and the corresponding force vectors were plotted during the upstroke ($4.0 \le \tau \le 4.5$) in Fig. 11. The magnitude and direction of the force vectors were directly influenced by lift and drag generated. The tilting of the force vector in the vertical direction means that the lift component is superior over the drag and an indication of better aerodynamic performance. The magnitude of the vector forces was higher for $\Delta\tau_\phi = 0.5$ in all the rigid cases than the flexible wings. One key observation was that the presence of wing flexibility caused the instantaneous force vectors to always tilt closer to the vertical direction than in the rigid wing case. Therefore, this behavior of the net forces for the flexible wing could be an indication of superior aerodynamic performance (L/D) than the rigid wing. This will be explained further using the net force angle.

The net force vector angle α_F was calculated from the angle between the force vector and the horizontal line. Eq. (7) shows that α_F is directly proportional to C_L/C_D, and could also be an indirect way to evaluate the performance of the wing. The α_F in Fig. 11 shows that the mean vector angle for the rigid wings is almost around 45° because the pressure forces acted perpendicular to the wing surface.

A critical examination of the effect of $\Delta\tau_\phi$ on α_F has been displayed in Fig. 12. First, the examination took into consideration how α_F was affected at the middle of the first ($\tau = 0.25$) and fifth ($\tau = 4.25$) half-strokes in Fig. 12(a) and (b), respectively. In the first half-stroke, the flow is void of any wake effect, but by the fifth stroke, the wake effect had reached its dynamic limit. The difference between the forces generated in the first and fifth cycles also comes from the acceleration from the impulsive start of the wing. Thus, the difference in force is not exclusively from the wake effect. In the absence of any wake at $\tau = 0.25$, α_F for the flexible wing showed a general increase as $\Delta\tau_\phi$ increased. The maximum difference in the increase in α_F was ∼8.12%. The rigid wing on the other hand showed only 1.12% drop in angle. With the onset of the wake, all the values of α_F almost converged to approximately the same value as seen in Fig. 12(b). The maximum variation was less than 1.4%. The rigid wing showed similar tendency with variation less than
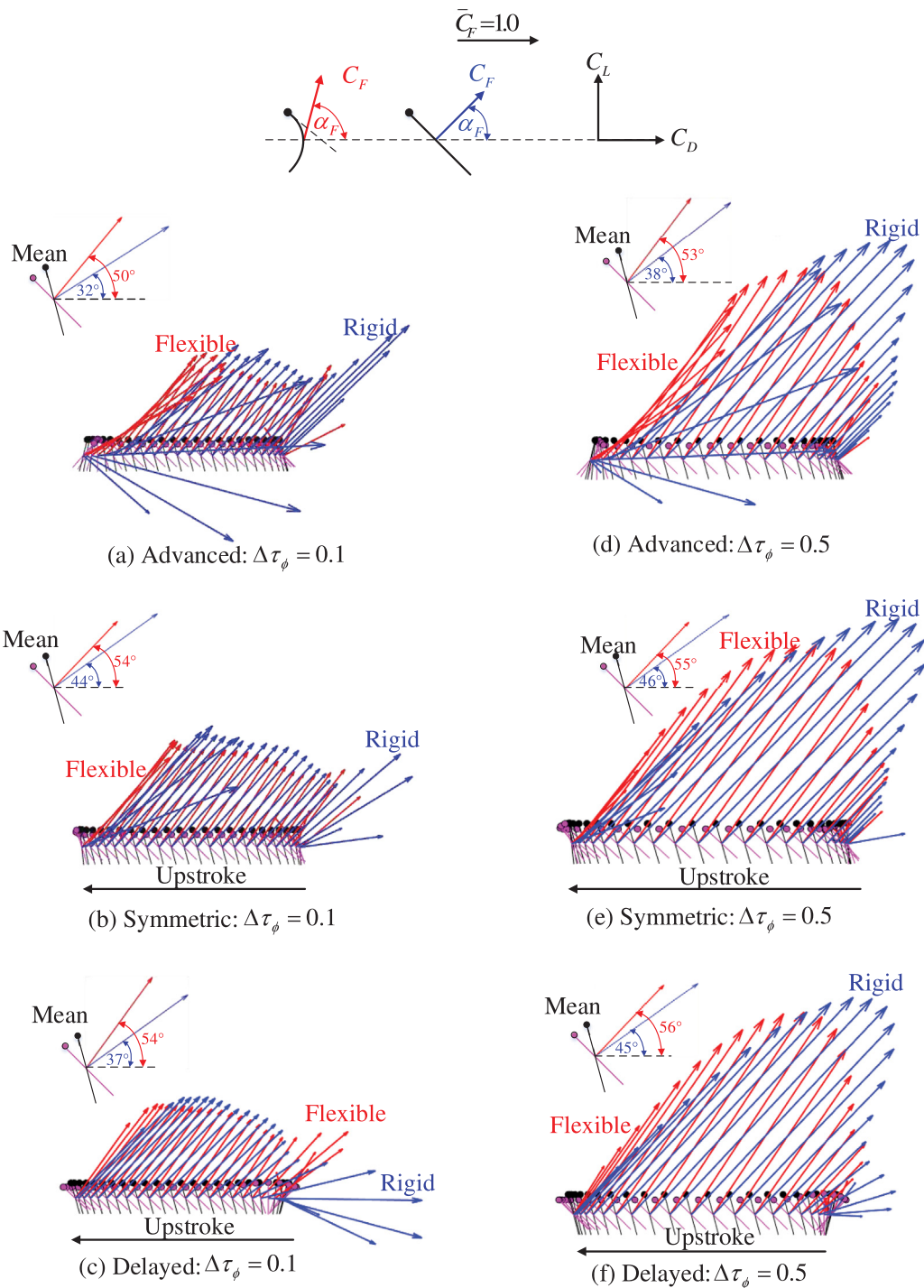
Fig. 11. Instantaneous net force vectors.

2%. Fig. 12(c) shows the results of α_F based on the entire fifth averaged-cycle. One key observation made was that the symmetric rotation for the rigid wing maintained a constant α_F while the delayed and advanced rotations increased with increasing $\Delta\tau_\phi$. Fig. 12(d) is basically a plot of α_F, which is indirectly proportional to L/D, against L/P for the variations of $\Delta\tau_\phi$ and τ_R. The advanced wing rotation performed the worst among the three wing rotations for both wings. Generally, an increase in $\Delta\tau_\phi$ increased the net force angle (L/D) and rather decreased the efficiency (L/P). This shows that careful considerations should be made when evaluating the aerodynamic performance of flapping wings. The use of L/P should
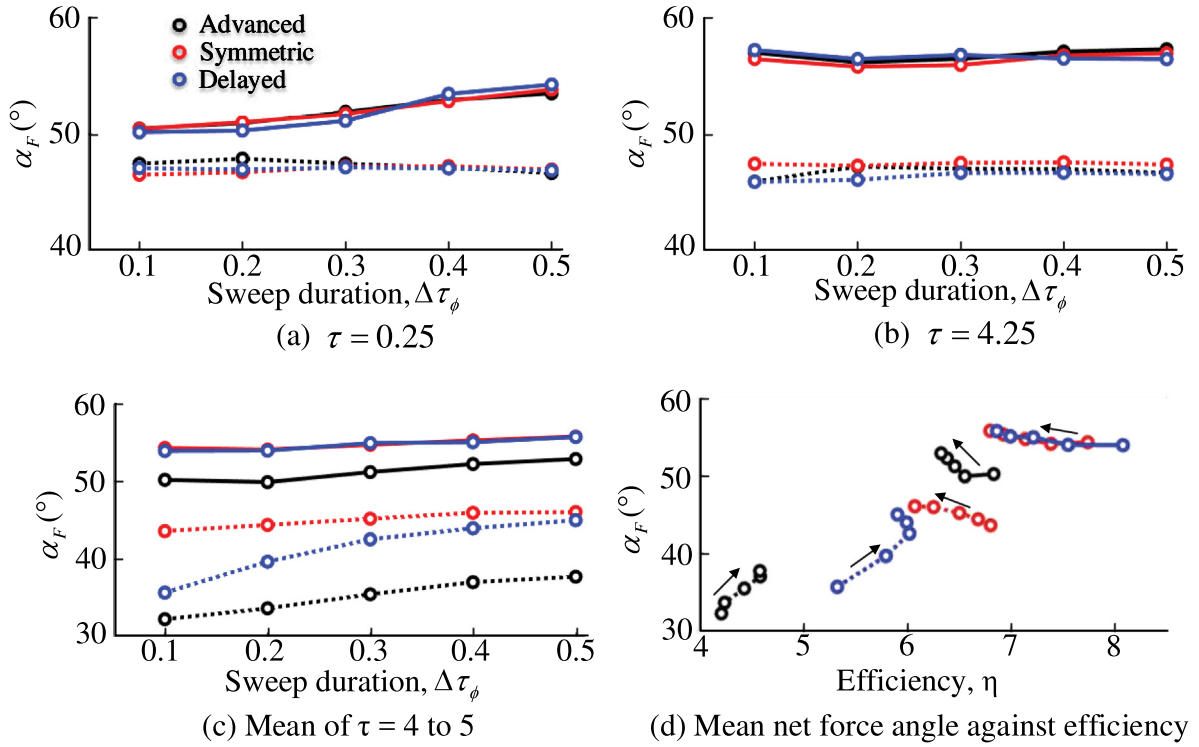
Fig. 12. Variation of the net force angle for each change in $\Delta\tau_\phi$ for the rigid (dash lines) and flexible (solid lines) wings. The arrows indicate an increase in $\Delta\tau_\phi$.

be a better approach as already explained in Section 4.1 of this study. Generally, the value of α_F could be higher in the flexible than rigid wing. This is an indication of a better aerodynamic performance as explained earlier, and could be the key role of wing flexibility in insect wing design.

$$\alpha_F = \tan^{-1}\left(\frac{C_L}{C_D}\right) \tag{7}$$

5. Instantaneous vortical structures (flow visualization)

In order to understand how the timing of wing rotation affects the vortical structures, the DPIV examination was considered for $\Delta\tau_\phi = 0.50$ with the flexible wing. The characteristics of the leading-edge (LEV) and the trailing-edge vortex (TEV) were investigated at $\tau = 4.60$ from 0.1b to 1.0b; ten cross-sections. At this time instant, the effect of the wing rotation on the generated forces was more distinct in Fig. 9b, and the $\phi(\tau)$ was 12.03° with $\theta(\tau)$ of 15°, 15°, and 4.35° for advanced, symmetric, and delayed rotations, respectively. This means that at this time instant the wing had completed the pitching motion with advanced and symmetric rotations. Normalization of the vorticities were achieved with Eq. (8). Fig. 13 shows that the LEV has not fully developed at this period. One interesting feature was that the underdeveloped LEV had formed across the entire wingspan except with delayed rotation. Here, the LEV had only formed at the outboard (~0.6b to 1.0b) section (refer to Fig. 19 in Appendix for the 3D view). In addition, it should be noted that the wing with delayed rotation was still in pitching motion at this period. Therefore, it could be seen from Fig. 13(c) that the outboard section of the wing had pitched in advance relative to the inboard section. This observation agrees with the report from Nakata and Liu (2012) for a twisted flexible wing in pitch motion. The delayed pitching at the inboard of the wing led to the incoherent LEV formation.

$$\hat{\omega} = \frac{\omega c}{U_{ref}} \tag{8}$$

The total first moment of vorticity in a fluid is directly proportional to the aerodynamic force produced in a flapping wing (Sun and Wu, 2004). The source of vorticity for the flapping wing is the LEV and TEV with opposing directions. From Fig. 13, the TEV1 was the main vortex since the LEV has not fully developed. The TEV1 for the advanced rotation had the strongest vorticity at this time instant, $\tau = 4.60$, and hence the highest lift. The subsequent reduction in the strength of the TEV1 caused a decrease in lift for the symmetric case. The lack of TEV1 formation for the delayed rotation means
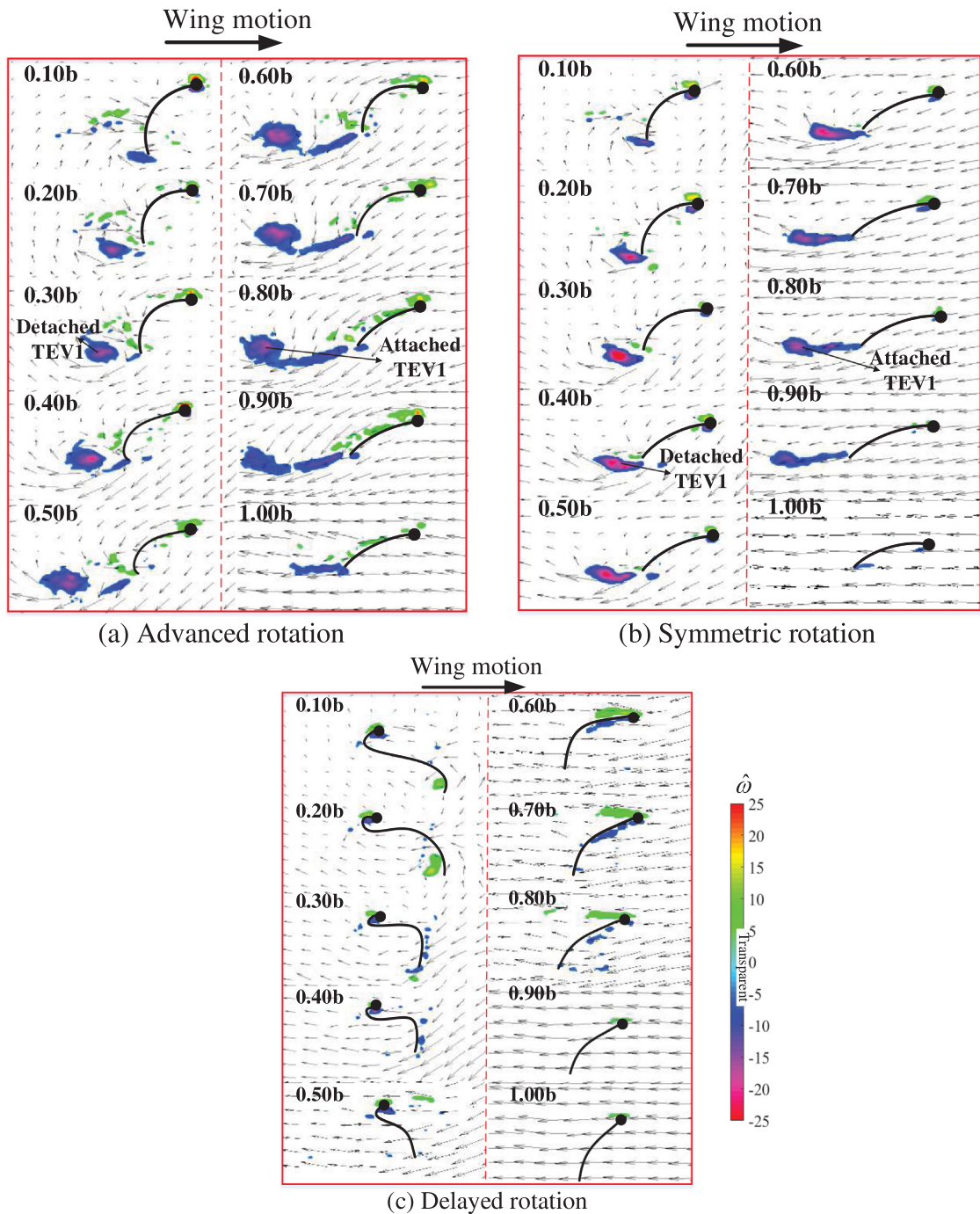
Fig. 13. Vortical structures at $\tau = 4.60$ for the flexible wing with $\Delta\tau_\phi = 0.50$.

that the lift generated could be attributed to the dissipation of the elastic energy, which will contribute to the steady and unsteady forces (Nakata and Liu, 2012), or other mechanisms that need further investigations. The elastic energy is reported to be stored as potential energy and released during this stage of the wing motion (Nakata and Liu, 2012; Reid et al., 2019). The shedding of the TEV1 varied across the wingspan. TEV1 was shed mostly at the inboard section while still attached at the outboard section ($\sim 0.6b$ to $1.0b$). This happened because of the twisted nature of the wing (to be discussed later).

Fig. 14 shows the vorticity distribution for the flexible and rigid wings at the middle of down stroke ($\tau = 4.75$) with $\Delta\tau_\phi = 0.1$. The effect of timing rotation was eliminated at this time instant because the individual wings had attained the
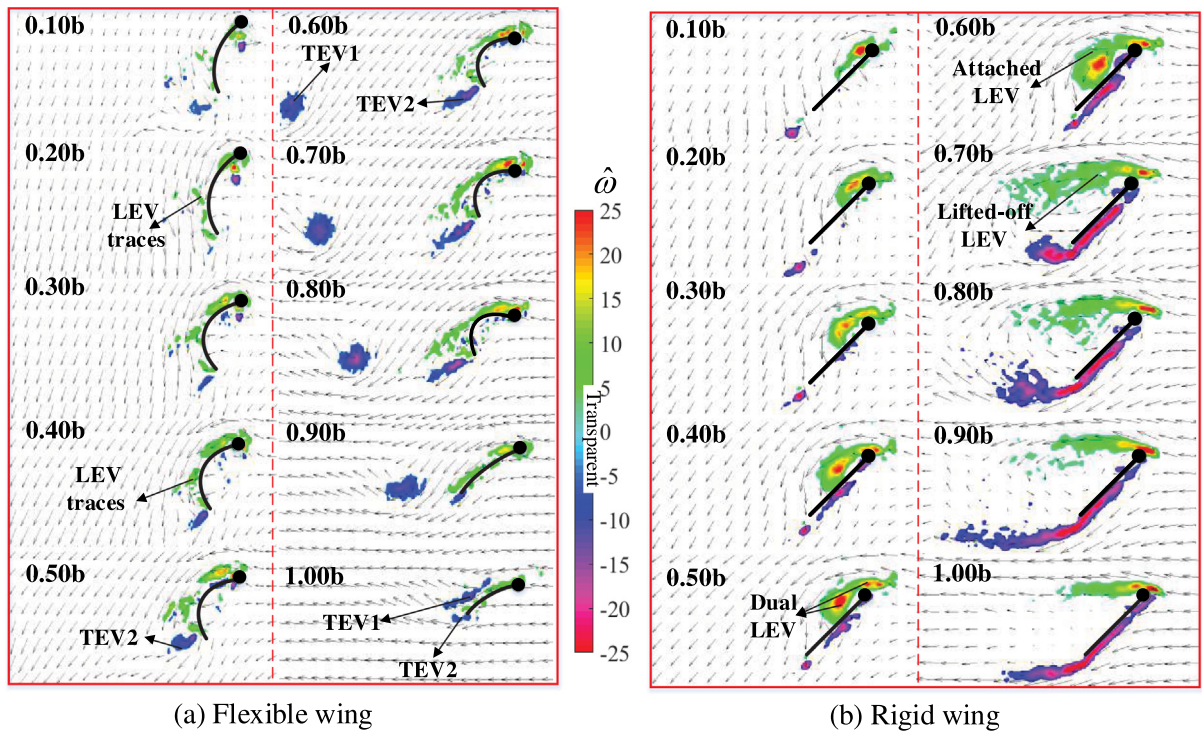
Fig. 14. Vortical structures across the wingspan at $\tau = 4.75$ with symmetric rotation and $\Delta\tau_\phi = 0.1$.

same pitch angle and velocity, which led to an approximately equal amount of lift generation. Therefore, the symmetric rotation was chosen for the comparison. The coherent LEV was found to be stable at the suction side of the rigid wing up to 0.6b with slight traces of the TEV as shown in Fig. 14(b). According to Fig. 4, this observation occurred at r*~3.6c, and agrees with the work from Kruyt et al. (2015). The dimensionless radial distances measured with respect to the chord and span are r^* and r, respectively, as shown in Fig. 5. The rolling of the TEV was slightly up from 0.7b to 1.0b. The flexible wing had similar conical distribution of the LEV as the rigid wing, but closely attached LEV to the surface of the wing.

The remarkable observation made in Fig. 14(a) was the behavior of the TEV. The proximity between TEV1 and TEV2 increased from the 0.6b to the wing tip. The appearance of TEV1 was noticed at that section of the wing because of the delay in the shedding of TEV1 as displayed in Fig. 13(b). This observation was more profound at the wing tip where the lack of TEV1 formation in Fig. 13(b) had resulted in the formation of both TEVs to be in very close proximity to the wing. The behavior of the TEV led to a slightly different flow-field around the two flapping wings. This clarifies the flexibility contribution in the flapping wing aerodynamics.

The sweep motion was changed to sinusoidal motion ($\Delta\tau_\phi = 0.5$) for both wings in Fig. 15. Here, the LEV had stronger vorticities compared to that in Fig. 14, which explains why $\Delta\tau_\phi = 0.5$ motion generated more lift than $\Delta\tau_\phi = 0.1$. For the rigid wing, the LEV was stable up to 0.5b contrary to the 0.6b in Fig. 14(b). This indicates that the change in $\Delta\tau_\phi$ could slightly affect the LEV stability. Multiple LEVs were noticed at the inboard section of the wing the flexible wing. The work of Yoon et al. (2020) also revealed these LEV traces, and they have been found to be affected by $\Delta\tau_\phi$ in this study (refer to Fig. 20 in Appendix for 3D view). The stretching of the LEV caused the creation of the dual-LEV (Lu et al., 2006). The dual-LEV was found from 0.3b to 0.5b and 0.5b to 0.9b for the rigid and flexible wings, respectively. The locations of the LEV stretching further shows how the flexible wing increased the LEV stability across the wingspan.

A comparison between the LEV for the rigid and flexible wings shows that the rigid wing generated stronger vorticity than the flexible wings in Figs. 14 and 15, which corresponded to the observed lift generated. These vorticities were far stronger and should have caused a very big difference in lift between the two wings. However, the difference was less than ~15% due to the presence of the counter-rotating pair vortex, which was created from the TEV1 and LEV, at the suction side of the flexible wing, and served as an additional mechanism to augment the lift. This pair vortex increased the momentum of the fluid, and could lead to the increase in sectional lift from 0.6b to 0.9b in Fig. 18b. Therefore, the vortex pair created by the flexible wing with twist could be an additional mechanism for enhancing the lift.

Extraction of some quantities were made from the DPIV results in Figs. 14 and 15 to help with the understanding of the characteristics of the wing deformation and the corresponding sectional lift. Since the deformation of the flexible wing was due to the FSI, an examination was first made to quantify how much of the chord length reduced for the generation of the positive camber as shown in Fig. 16(a). The reduction was expressed as a percentage of the actual chord length and
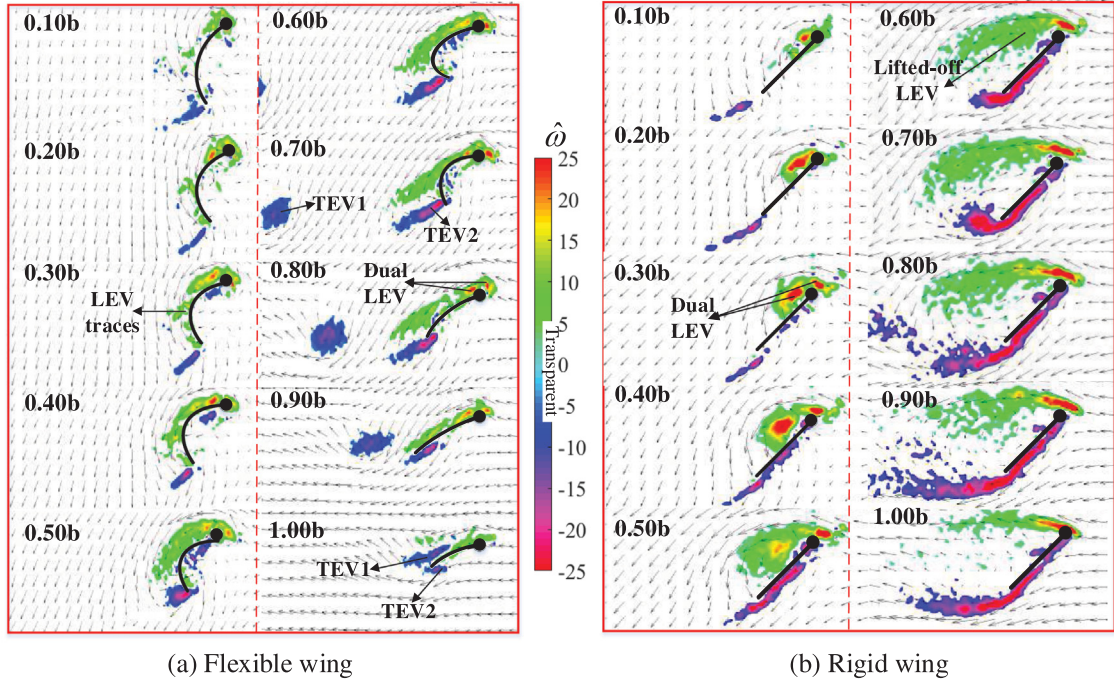
Fig. 15. Vortical structures across the wingspan at $\tau = 4.75$ with symmetric rotation and $\Delta\tau_\phi = 0.5$.
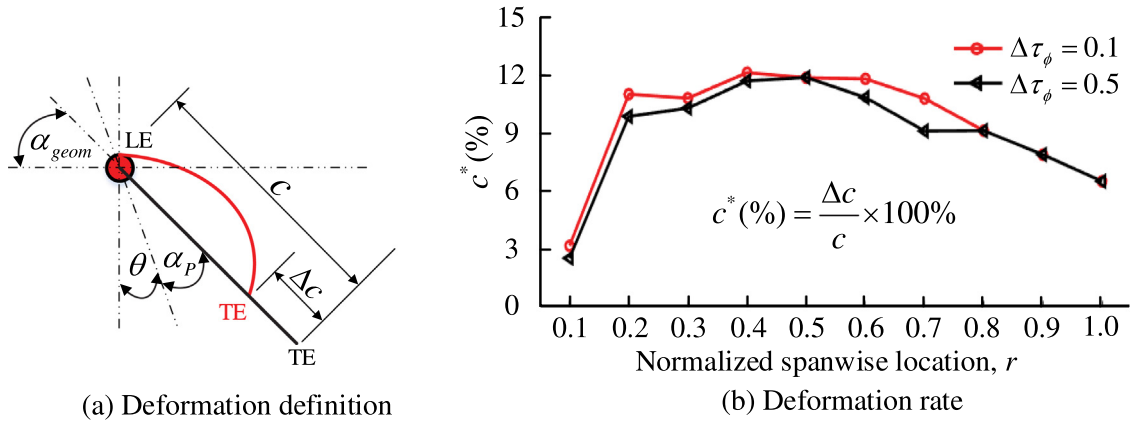

Fig. 16. Deformation of the flexible wing based on the reduced chord length at $\tau = 4.75$.

termed, deformation rate c^*. The result in Fig. 16(b) shows that the c^* varied across the wingspan, which is an indication of varied camber across the span. The maximum c^* occurred at the mid-span; ~12%. From 0.6b to 1.0b, the wing began to experience a decrease in c^* because the effect of the wing root constraint on the wing deformation kept reducing. For instance, the wingtip could be aligned freely with the flow leading to a drastic reduction in α_{geom} compared to the α_{geom} at the wing root. The lowest c^* occurred at the wing root because of the constraint created by the root vein.

The velocities of the flow in the x- and z-directions, u_i and w_i, were used to calculate the freestream velocities U_{inflow}. These quantities were extracted from 1.3c ahead of the wing (refer to the insert in Fig. 17). This approach was adopted from the study by Han et al. (2019). The freestream velocities were normalized with the sectional velocity U_{sec}, which was computed as the local velocity at each section of the wing, as presented in Eq. (9). The induced α_{ind} and effective α_{eff} angles of attack were calculated using Eqs. (10) and (11).

$$\frac{U_{inflow}}{U_{sec}} = \frac{1}{N}\sum_{i=1}^{N}\frac{\sqrt{w_i^2 + (U_{sec} + u_i)^2}}{U_{sec}} \tag{9}$$

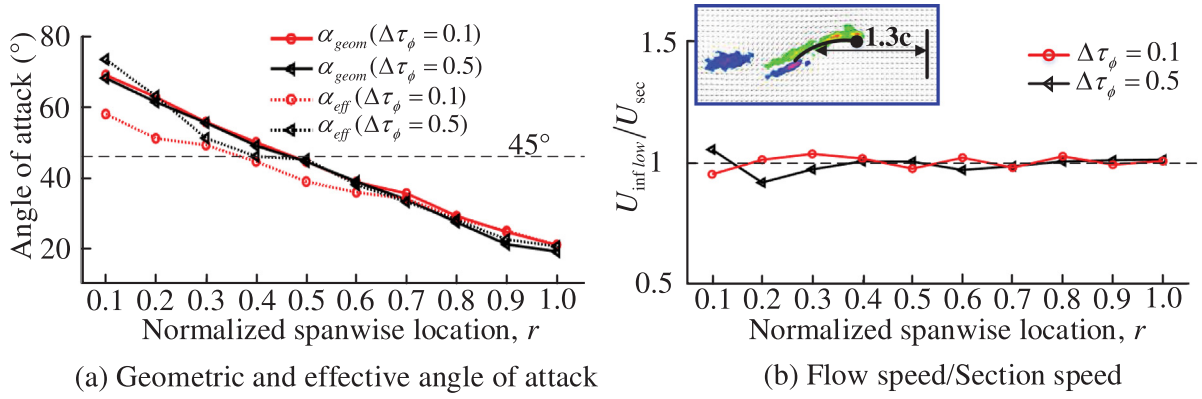(a) Geometric and effective angle of attack

(b) Flow speed/Section speed

Fig. 17. Variation of the angle of attack and inflow velocity across the wingspan of the flexible wing at $\tau = 4.75$.

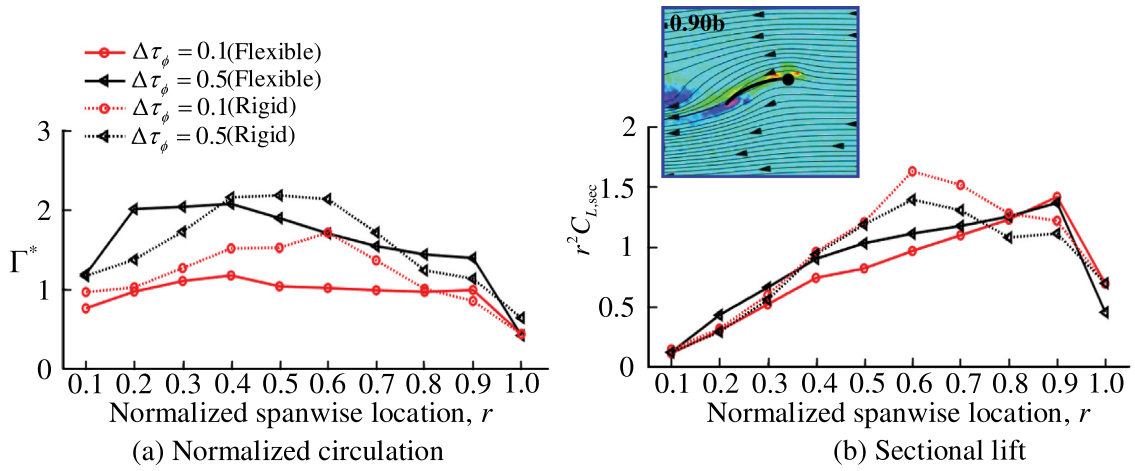

(a) Normalized circulation

(b) Sectional lift

Fig. 18. Normalized circulation and sectional lift across the wingspan at $\tau = 4.75$.

$$\alpha_{ind} = \frac{1}{N} \sum_{i=1}^{N} \tan^{-1} \frac{w_i}{U_{sec} + u_i} \qquad (10)$$

$$\alpha_{eff} = \alpha_{geom} - \alpha_{ind} \qquad (11)$$

The variation of $\Delta\tau_\phi$ for the flexible wing had a minimal effect on α_{geom} at $\tau = 4.75$ as shown in Fig. 17(a). The α_{geom} decreased linearly from the wing root to tip as already reported in literature (Phan et al., 2017a). This is an indication of negative geometric twist, and a typical feature in the wing deformation of natural flyers (Walker et al., 2010; Young et al., 2009; Truong et al., 2012). The study from Phan et al. (2017a) showed that an increase in the twist from ∼8° to ∼45° could decrease the power consumption by ∼23.3% in comparison with a flat flexible wing at 0.50b. Therefore, the linear twist of ∼55° in this study was responsible for the low power consumption by the flexible wing, and supports the findings in literature (Phan et al., 2017a; Young et al., 2009; Nakata and Liu, 2012; Du and Sun, 2010). The plot of α_{eff} using Eq. (11) displayed the same linear behavior as shown in Fig. 17(a). The variation of $\Delta\tau_\phi$ had a slight effect on α_{eff} especially from 0.1b to 0.3b. The higher U_{inflow} than U_{sec} at 0.1b for $\Delta\tau_\phi = 0.1$ caused the observed increase in α_{eff} at that section of the wing as shown in Fig. 17(b).

The lift enhancement by the LEV can be calculated from the circulatory forces (Ansari et al., 2006). Therefore, the evaluation of the LEV growth at each cross-section was performed by calculating the circulation Γ and sectional lift. The maximum circulation around the wing was normalized in Eq. (12), and used to calculate the circulation sectional lift $C_{L,sec}$ in Eq. (13). Fig. 18 shows the results of Γ^* and $C_{L,sec}r^2$ against the normalized spanwise location r conducted at $\tau = 4.75$ with $\Delta\tau_\phi = 0.1$ and 0.5 for both wings.

$$\Gamma^* = \frac{\Gamma}{cU_{ref}} \qquad (12)$$

$$C_{L,\text{sec}} = \frac{2\Gamma}{U_{\text{sec}}c} \tag{13}$$

The $\Delta\tau_\phi = 0.5$ motion generated more lift at each cross-section than $\Delta\tau_\phi = 0.1$ for both wings at $\tau = 4.75$. The flexible wing generated higher lift than rigid wing at the inboard section of the wing from 0.1b to 0.3b and at the near-tip region as shown in the Fig. 18(a). The results in Fig. 18(b) show that $C_{L,\text{sec}} \sim 1/r$, and agrees with literature (Kweon and Choi, 2010). The plot in Fig. 18(b) shows a drop in the vortex lift at 0.60b and 0.90b for the rigid and flexible wing, respectively, regardless the change in $\Delta\tau_\phi$. This implies that the radial limit of delayed stall was increased from $r^* = 3.8c$ in the rigid case to 4.8c in the flexible case (refer to Fig. 5 for r^* definition). As also shown in the insert in Fig. 18(b), the streamlines around the flexible wing at 0.90b gradually merged at the trailing-edge to satisfy the Kutta condition. The low α_{geom} at the outboard section of the flexible wing, which was less than 45° from 0.60b to 1.0b according to Fig. 17(a), helped to stabilize the LEV in comparison to the LEV of the rigid wing at the same sections. This implies that the presence of negative geometric twist in insect wing deformation plays a significant role by helping to stabilize the LEV, and a subsequent delay in the bursting of the LEV (Nakata and Liu, 2012).

6. Conclusion

This paper investigated the contributions of two wing kinematic parameters in enhancing the aerodynamic performance of rigid and flexible flapping wings. The flexible wing deployed in this study had similar deformation as found in natural flyers and some FWMAVs; linear twist and positive camber. The piecewise wing kinematics method was adopted to vary the timing of wing rotation and sweep motion duration of the wing. The aerodynamic forces were collected from a six-axis sensor attached to a scaled-up robotic model immersed into a water-tank environment.

The study found the timing of wing rotation to have stronger effect on the aerodynamic characteristics of the rigid wing than the flexible case. The aerodynamic characteristics of the flexible wing rather displayed a conspicuous phase delay irrespective of the timing rotation. This delay was found to be very sensitive to the variation of the sweep duration. Generally, an increase in the sweep duration increased the lift generated by both wings.

This study revealed that wing flexibility could increase the lift generated at the end of stroke by releasing its stored elastic energy, which is in the form of camber and twist. In addition, the presence of wing flexibility totally eliminated the generation of transient negative lift, which has been established in literature for the rigid wing undergoing delayed and advanced rotations. The adoption of the sinusoidal sweep motion was observed to be a better way to reduce the magnitude of the negative lift for the rigid wing. Further examination revealed that the instantaneous and net force vectors of the flexible wing were tilted in an upward position compared to the rigid case. This caused the net force angle, which was directly proportional to the ratio of lift to drag, to be higher for the flexible case, and have a better aerodynamic performance than the rigid wing.

The vortical structures around the flexible wing were observed to be slightly different from those around the rigid wing. The DPIV results showed a decrease in proximity between the flexible wing and its shed TEV. This occurred from 0.60b to 1.0b because the angle of attack at those sections were less than 45°. This linear twist caused the LEV at the outboard section of the wing to be strongly attached to the wing surface. Therefore, the flexible wing increased the radial limit of the delayed stall from 3.6c in the rigid wing to 4.8c. The study has shown that the presence of negative geometric twist in insect wing deformation plays a significant role by stabilizing the LEV, and causing a subsequent delay in the LEV burst.

Declaration of competing interest

The authors declare that they have no known competing financial interests or personal relationships that could have appeared to influence the work reported in this paper.

Acknowledgments

Appendix. Re-construction of DPIV results into 3D view

The two-dimensional (2D) vortical structures were re-constructed in a three-dimensional (3D) space for better understanding and simplification of the view. The rigid wing was used to represent all cases only for demonstration purpose.
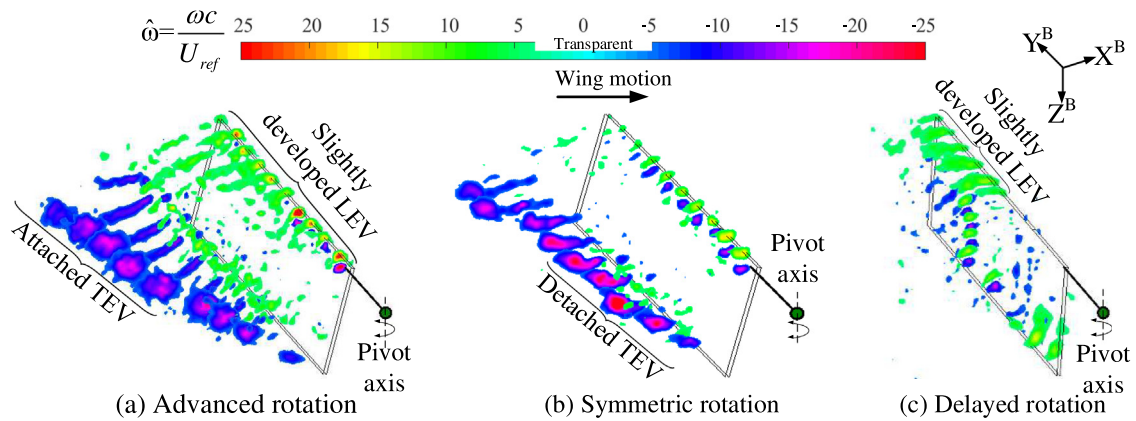
Fig. 19. 3D view of vorticity distribution on the flexible wing for varied timing of duration at $\tau = 4.60$.
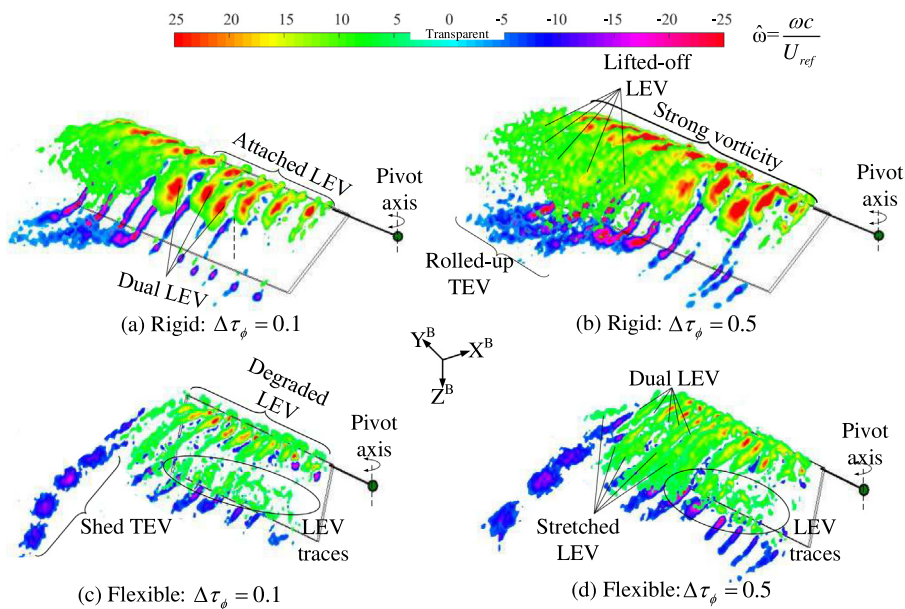

Fig. 20. 3D view comparison of the vortical structures for the wings undergoing symmetric rotation at $\tau = 4.75$.

References

Addo-Akoto, R., Han, J.S., Han, J.H., 2019. Influence of aspect ratio on wing–wake interaction for flapping wing in hover. Exp. Fluids 60, 1–18. http://dx.doi.org/10.1007/s00348-019-2816-0.

Addo-Akoto, R., Han, J.S., Han, J.H., 2020. Aerodynamic performance of flexible flapping wings deformed by slack angle. Bioinspir. Biomim. http://dx.doi.org/10.1088/1748-3190/aba8ac.

Addo-Akoto, R., Han, J.H., Han, J.S., 2021. Effects of sweep-motion profile on rigid and flexible flapping-wing aerodynamics. In: AIAA Scitech 2021 Forum. pp. 1–14. http://dx.doi.org/10.2514/6.2021-0225.

Altshuler, D.L., Dickson, W.B., Vance, J.T., Roberts, S.P., Dickinson, M.H., 2005. Short-amplitude high-frequency wing strokes determine the aerodynamics of honeybee flight. Proc. Natl. Acad. Sci. USA 102, 18213–18218. http://dx.doi.org/10.1073/pnas.0506590102.

Ansari, S.A., Zbikowski, R., Knowles, K., 2006. Aerodynamic modelling of insect-like flapping flight for micro air vehicles. Prog. Aerosp. Sci. 42, 129–172. http://dx.doi.org/10.1016/j.paerosci.2006.07.001.

Berman, G.J., Wang, Z.J., 2007. Energy-minimizing kinematics in hovering insect flight. J. Fluid Mech. 582, 153–168. http://dx.doi.org/10.1017/S0022112007006209.

Bhat, S.S., Zhao, J., Sheridan, J., Hourigan, K., Thompson, M.C., 2020. Effects of flapping-motion profiles on insect-wing aerodynamics. J. Fluid Mech. 884, http://dx.doi.org/10.1017/jfm.2019.929.

Birch, J.M., Dickinson, M.H., 2001. Spanwise flow and the attachment of the leading-edge vortex on insect wings. Nature 412, 729–733. http://dx.doi.org/10.1038/35089071.

Birch, J.M., Dickinson, M.H., 2003. The influence of wing-wake interactions on the production of aerodynamic forces in flapping flight. J. Exp. Biol. 206, 2257–2272. http://dx.doi.org/10.1242/jeb.00381.

Chin, D.D., Lentink, D., 2016. Flapping wing aerodynamics: from insects to vertebrates. J. Exp. Biol. 219, 920–932. http://dx.doi.org/10.1242/jeb.042317.

Dai, H., Luo, H., Doyle, J.F., 2012. Dynamic pitching of an elastic rectangular wing in hovering motion. J. Fluid Mech. 693, 473–499. http://dx.doi.org/10.1017/jfm.2011.543.

Dickinson, M.H., Lehmann, F.O., Sane, S.P., 1999. Wing rotation and the aerodynamic basis of insect flight. Science 284, 1954–1960. http://dx.doi.org/10.1126/science.284.5422.1954.

Du, G., Sun, M., 2008. Effects of unsteady deformation of flapping wing on its aerodynamic forces. Appl. Math. Mech. (English Ed.) 29, 731–743. http://dx.doi.org/10.1007/s10483-008-0605-9.

Du, G., Sun, M., 2010. Effects of wing deformation on aerodynamic forces in hovering hoverflies. J. Exp. Biol. 213, 2273–2283. http://dx.doi.org/10.1242/jeb.040295.

Ellington, C.P., 1984. The aerodynamics of hovering insect flight. III. Kinematics. Phil. Trans. R. Soc. B 305, 41–78. http://dx.doi.org/10.1098/rstb.1984.0051.

Ennos, A.R., 1988. The inertial cause of wing rotation in diptera. J. Exp. Biol. 140, 161–169.

Fry, S.N., Sayaman, R., Dickinson, M.H., 2005. The aerodynamics of hovering flight in Drosophila. J. Exp. Biol. 208, 2303–2318. http://dx.doi.org/10.1242/jeb.01612.

Fu, J., Liu, X., Shyy, W., Qiu, H., 2018. Effects of flexibility and aspect ratio on the aerodynamic performance of flapping wings. Bioinspir. Biomim. 13, 036001. http://dx.doi.org/10.1088/1748-3190/aaaac1.

Garmann, D.J., Visbal, M.R., Orkwis, P.D., 2013. Three-dimensional flow structure and aerodynamic loading on a revolving wing. Phys. Fluids 25, http://dx.doi.org/10.1063/1.4794753.

Gu, M., Wu, J., Zhang, Y., 2020. Wing rapid responses and aerodynamics of fruit flies during headwind gust perturbations. Bioinspir. Biomim. 15, http://dx.doi.org/10.1088/1748-3190/ab97fc.

Han, J.S., Chang, J.W., Kim, S.T., 2014. Reynolds number dependency of an insect-based flapping wing. Bioinspir. Biomim. 9, http://dx.doi.org/10.1088/1748-3182/9/4/046012.

Han, J.S., Chang, J.W., Kim, J.K., Han, J.H., 2015a. Role of trailing-edge vortices on the hawkmothlike flapping wing. J. Aircr. 52, 1256–1266. http://dx.doi.org/10.2514/1.C032768.

Han, J.S., Kim, J.K., Chang, J.W., Han, J.H., 2015b. An improved quasi-steady aerodynamic model for insect wings that considers movement of the center of pressure. Bioinspir. Biomim. 10, 46014. http://dx.doi.org/10.1088/1748-3190/10/4/046014.

Han, J.S., Kim, H.Y., Han, J.H., 2019. Interactions of the wakes of two flapping wings in hover. Phys. Fluids 31, http://dx.doi.org/10.1063/1.5078669.

Harbig, R.R., Sheridan, J., Thompson, M.C., 2013. Relationship between aerodynamic forces, flow structures and wing camber for rotating insect wing planforms. J. Fluid Mech. 730, 52–75. http://dx.doi.org/10.1017/jfm.2013.335.

Kang, C.K., Shyy, W., 2013. Scaling law and enhancement of lift generation of an insect-size hovering flexible wing. J. R. Soc. Interface 10, http://dx.doi.org/10.1098/rsif.2013.0361.

Kruyt, J.W., Van Heijst, G.J.F., Altshuler, D.L., Lentink, D., 2015. Power reduction and the radial limit of stall delay in revolving wings of different aspect ratio. J. R. Soc. Interface 12, http://dx.doi.org/10.1098/rsif.2015.0051.

Kweon, J., Choi, H., 2010. Sectional lift coefficient of a flapping wing in hovering motion. Phys. Fluids 22, 1–4. http://dx.doi.org/10.1063/1.3471593.

Kweon, J., Choi, H., 2012. Three-dimensional flows around a flapping wing in ground effect. In: 7th Int. Conf. Comput. Fluid Dyn., ICCFD 2012, pp. 4–5.

Liu, Y., Sun, M., 2008. Wing kinematics measurement and aerodynamics of hovering droneflies. J. Exp. Biol. 211, 2014–2025. http://dx.doi.org/10.1242/jeb.016931.

Lu, Y., Gong, X.S., Guo, J.L., 2006. Dual leading-edge vortices on flapping wings. J. Exp. Biol. 209, 5005–5016. http://dx.doi.org/10.1242/jeb.02614.

Lua, K.B., Lim, T.T., Yeo, K.S., 2014. Scaling of aerodynamic forces of three-Dimensional flapping wings. AIAA J. 52, 1095–1101. http://dx.doi.org/10.2514/1.J052730.

Nabawy, M.R.A., Crowther, W.J., 2015. Aero-optimum hovering kinematics. Bioinspir. Biomim. 10, http://dx.doi.org/10.1088/1748-3190/10/4/044002.

Nakata, T., Liu, H., 2012. Aerodynamic performance of a hovering hawkmoth with flexible wings: A computational approach. Proc. R. Soc. B Biol. Sci. 279, 722–731. http://dx.doi.org/10.1098/rspb.2011.1023.

Nan, Y., Karásek, M., Lalami, M.E., Preumont, A., 2017. Experimental optimization of wing shape for a hummingbird-like flapping wing micro air vehicle. Bioinspir. Biomim. 12, http://dx.doi.org/10.1088/1748-3190/aa5c9e.

Nguyen, Q.V., Chan, W.L., 2019. Development and flight performance of a biologically-inspired tailless flapping-wing micro air vehicle with wing stroke plane modulation. Bioinspir. Biomim. 14, http://dx.doi.org/10.1088/1748-3190/aaefa0.

Nguyen, T.T., Shyam Sundar, D., Yeo, K.S., Lim, T.T., 2016. Modeling and analysis of insect-like flexible wings at low Reynolds number. J. Fluids Struct. 62, 294–317. http://dx.doi.org/10.1016/j.jfluidstructs.2016.01.012.

O'Hara, R.P., Palazotto, A.N., 2012. The morphological characterization of the forewing of the Manduca sexta species for the application of biomimetic flapping wing micro air vehicles. Bioinspir. Biomim. 7, http://dx.doi.org/10.1088/1748-3182/7/4/046011.

Phan, H.V., Kang, T., Park, H.C., 2017b. Design and stable flight of a 21 g insect-like tailless flapping wing micro air vehicle with angular rates feedback control. Bioinspir. Biomim. 12, http://dx.doi.org/10.1088/1748-3190/aa65db.

Phan, H.V., Truong, Q.T., Park, H.C., 2017a. An experimental comparative study of the efficiency of twisted and flat flapping wings during hovering flight. Bioinspir. Biomim. 12, http://dx.doi.org/10.1088/1748-3190/aa65e6.

Ramamurti, R., Sandberg, W.C., 2002. A three-dimensional computational study of the aerodynamic mechanisms of insect flight. J. Exp. Biol. 205, 1507–1518.

Reid, H.E., Schwab, R.K., Maxcer, M., Peterson, R.K.D., Johnson, E.L., Jankauski, M., 2019. Wing flexibility reduces the energetic requirements of insect flight. Bioinspir. Biomim. 14, http://dx.doi.org/10.1088/1748-3190/ab2dbc.

Roshanbin, A., Abad, F., Preumont, A., 2019. Kinematic and aerodynamic enhancement of a robotic hummingbird. AIAA J. 1–9. http://dx.doi.org/10.2514/1.J057737.

Roshanbin, A., Altartouri, H., Karásek, M., Preumont, A., 2017. COLIBRI: A hovering flapping twin-wing robot. Int. J. Micro Air Veh. 9, 270–282. http://dx.doi.org/10.1177/1756829317695563.

Ryu, Y.G., Chang, J.W., Chung, J., 2019. Aerodynamic characteristics of flexible wings with leading-edge veins in pitch motions. Aerosp. Sci. Technol. 86, 558–571. http://dx.doi.org/10.1016/j.ast.2019.01.013.

Sane, S.P., Dickinson, M.H., 2001. The control of flight force by a flapping wing: Lift and drag production. J. Exp. Biol. 204, 3401.

Sane, S.P., Dickinson, M.H., 2002. The aerodynamic effects of wing rotation and a revised quasi-steady model of flapping flight. J. Exp. Biol. 205, 1087–1096.

Shyy, W., Aono, H., Chimakurthi, S.K., Trizila, P., Kang, C.K., Cesnik, C.E.S., Liu, H., 2010. Recent progress in flapping wing aerodynamics and aeroelasticity. Prog. Aerosp. Sci. 46, 284–327. http://dx.doi.org/10.1016/j.paerosci.2010.01.001.

Shyy, W., Aono, H., Kang, C.K., Liu, H., 2013. An Introduction to Flapping Wing Aerodynamics. Cambridge University Press, Cambridge.

Shyy, W., Liu, H., 2007. Flapping wings and aerodynamic lift: the role of leading-edge vortices. AIAA J. 45, 2817–2819. http://dx.doi.org/10.2514/1.33205.

Sridhar, M., Kang, C.K., 2015. Aerodynamic performance of two-dimensional, chordwise flexible flapping wings at fruit fly scale in hover flight. Bioinspir. Biomim. 10, 1–14. http://dx.doi.org/10.1088/1748-3190/10/3/036007.

Sun, M., Tang, J., 2002. Unsteady aerodynamic force generation by a model fruit fly wing in flapping motion. J. Exp. Biol. 205, 55–70.

Sun, M., Wu, J., 2004. Large aerodynamic forces on a sweeping wing at low Reynolds number. Acta Mech. Sin. 20, 24–31. http://dx.doi.org/10.1007/bf02484241.

Thielicke, W., Stamhuis, E.J., 2014. PIVlab – Towards user-friendly, affordable and accurate digital particle image velocimetry in MATLAB. J. Open Res. Softw. 2, http://dx.doi.org/10.5334/jors.bl.

Truong, T.V., Le, T.Q., Byun, D., Park, H.C., Kim, M., 2012. Flexible wing kinematics of a free-flying beetle (rhinoceros beetle trypoxylus dichotomus). J. Bionic Eng. 9, 177–184. http://dx.doi.org/10.1016/S1672-6529(11)60113-3.

Walker, S.M., Thomas, A.L.R., Taylor, G.K., 2010. Deformable wing kinematics in free-flying hoverflies. J. R. Soc. Interface 7, 131–142. http://dx.doi.org/10.1098/rsif.2009.0120.

Wang, Q., Goosen, J.F.L., van Keulen, F., 2017. An efficient fluid–structure interaction model for optimizing twistable flapping wings. J. Fluids Struct. 73, 82–99. http://dx.doi.org/10.1016/j.jfluidstructs.2017.06.006.

Wieneke, B., 2015. PIV uncertainty quantification from correlation statistics. Meas. Sci. Technol. 26, http://dx.doi.org/10.1088/0957-0233/26/7/074002.

Wootton, R.J., 1990. The mechanical design of insect wings. Sci. Am. 263, 114–120. http://dx.doi.org/10.1038/scientificamerican1190-114.

Yoon, S.H., Cho, H., Lee, J., Kim, C., Shin, S.J., 2020. Effects of camber angle on aerodynamic performance of flapping-wing micro air vehicle. J. Fluids Struct. 97, http://dx.doi.org/10.1016/j.jfluidstructs.2020.103101.

Young, J., Walker, S.M., Bomphrey, R.J., Taylor, G.K., Thomas, A.L.R., 2009. Details of insect wing design and deformation enhance aerodynamic function and flight efficiency. Science 325, 1549–1552. http://dx.doi.org/10.1126/science.1175928.

Zhao, L., Huang, Q., Deng, X., Sane, S.P., 2010. Aerodynamic effects of flexibility in flapping wings. J. R. Soc. Interface 7, 485–497. http://dx.doi.org/10.1098/rsif.2009.0200.